

# JGR Earth Surface

## RESEARCH ARTICLE

10.1029/2021JF006532

### Key Points:

- Oversnow radar data reveals the shape of a subglacially sourced basal channel at the grounding line of the Kamb Ice Stream
- Remote sensing suggests that more than 35 m/a melt occurs at the upstream tip of the channel, and shows that the channel is growing upstream
- Repeat autonomous phase-sensitive radio-echo sounder surveying shows accretion across the channel downstream from the channels inception

### Supporting Information:

Supporting Information may be found in the online version of this article.

### Correspondence to:

A. Whiteford,  
arranjcw@gmail.com

### Citation:

Whiteford, A., Horgan, H. J., Leong, W. J., & Forbes, M. (2022). Melting and refreezing in an ice shelf basal channel at the grounding line of the Kamb Ice Stream, West Antarctica. *Journal of Geophysical Research: Earth Surface*, 127, e2021JF006532. <https://doi.org/10.1029/2021JF006532>

Received 20 NOV 2021

Accepted 10 OCT 2022

## Melting and Refreezing in an Ice Shelf Basal Channel at the Grounding Line of the Kamb Ice Stream, West Antarctica

A. Whiteford<sup>1</sup> , H. J. Horgan<sup>1</sup> , W. J. Leong<sup>2</sup> , and M. Forbes<sup>3</sup>

<sup>1</sup>Antarctic Research Centre, Victoria University of Wellington, Wellington, New Zealand, <sup>2</sup>Byrd Polar and Climate Research Centre, Ohio State University, Columbus, OH, USA, <sup>3</sup>School of Surveying, University of Otago, Dunedin, New Zealand

**Abstract** Ice shelves buttress ice streams and glaciers, slowing the rate at which they flow into the ocean. When this buttressing is reduced, either through increased melt or calving, the increased discharge of grounded ice upstream contributes to sea level rise. The thickness, strength, and stability of ice shelves can be influenced by channels in the ice base. Here, we focus on a subglacially sourced basal channel which is observed to have melted up to 50% of the ice shelf thickness. The channel extends 6 km upstream of the previously estimated grounding line of the stagnant Kamb Ice Stream. Using a combination of ground-based observations and remote sensing, we find that the channel is growing upstream over time. Over-snow radar surveying images the shape of the channel, constrains a steep inception, and shows that not all of the basal shape is manifest at the surface. Modern surface lowering at the upstream head of the channel is interpreted as a region of focused melt where a subglacial outlet meets the ocean cavity. We estimate this basal melt to be at least 35 m/a in a narrow (200 m × 1.5 km) zone. Downstream from the melt region, repeat phase sensitive radar observations reveal accretion contributing to the growth of a ledge on the true-right side of the channel. We conclude that the channel is likely formed by a retreating subglacial outlet which enhances basal melt episodically.

**Plain Language Summary** Ice flows off the Antarctic continent and floats on the surrounding ocean, forming ice shelves. These ice shelves get stuck against the Antarctic coastline and islands, blocking ice flow from the continent to the open ocean. When ice shelves break apart or thin by melting, they have less ability to block ice flow. As a result, more ice flows from the continent into the ocean resulting in sea level rise. Melting can be especially strong in channels which form underneath floating ice. This paper focuses on a channel melted into the base of the Ross Ice Shelf at the inland coastline. We used radar to map the channel and found that it has a similar shape to a river mouth, though under approximately 350 m of ice. Water from the Antarctic continent flows to the ocean through this channel. Using data from satellites we found an area on the ice surface above the channel which is lowering, likely because of melting in the channel underneath. We estimated that the ice base is melting by at least 35 m per year in a narrow zone. Downstream, we used radar to find that in the channel water is freezing to the base of the ice shelf.

## 1. Introduction

### 1.1. Ice Shelves

Accelerating ice loss from Antarctica's ice sheets is projected to contribute 13–42 cm of sea level rise by the end of the century (Edwards et al., 2021). This contribution is mainly driven by an increase in ice flowing off the continent and into the ocean. Most Antarctic ice discharge becomes part of a floating ice shelf (Rignot et al., 2013), half of which will melt before it reaches the open ocean, while the other half will eventually calve as icebergs (Liu et al., 2015; Rignot et al., 2013). Ice shelves slow the discharge of glacial ice into the ocean. When ice shelves drag past coastlines, islands, and pinning points, they generate back stresses and buttress against ice flow (e.g., Dupont & Alley, 2005; Fürst et al., 2016). This buttressing is an important control on the rate of ice loss from Antarctica. The removal of buttressing when an ice shelf retreats or disintegrates leads to the acceleration of ice loss (e.g., Berthier et al., 2012; Rignot et al., 2004; Scambos et al., 2004).

Melt at the base of ice shelves is largely controlled by ocean circulation in the sub-ice-shelf cavity. Theoretical frameworks of ocean circulation under ice shelves were first developed from the interpretation of direct oceanographic observations at ice shelf fronts (e.g., S. S. Jacobs et al., 1979). At a large scale, currents under an ice shelf follow a circulation-cell, described in detail by S. Jacobs et al. (1992) and well approximated by the ice pump mechanism (Lewis & Perkin, 1986). Sea ice formation releases high salinity water which sinks and flows down-

© 2022. The Authors.

This is an open access article under the terms of the [Creative Commons Attribution-NonCommercial-NoDerivs License](https://creativecommons.org/licenses/by-nc-nd/4.0/), which permits use and distribution in any medium, provided the original work is properly cited, the use is non-commercial and no modifications or adaptations are made.

slope along the seafloor into the ice shelf cavity. This relatively dense, warm water comes into contact with the ice shelf at the grounding line, where it melts the ice shelf base and forms a meltwater plume. The fresh, buoyant plume (described in a 1d model by Jenkins (1991)) flows along the ice–ocean interface to the open ocean. This theory predicts ice shelf melt to be strongest at two places: near the ice shelf front where ice is in close contact with the open ocean, and in the region near the grounding line where the relatively warm water from the lowest portion of the water column meets the ice shelf. Near the grounding line, stronger tidal mixing and the development of meltwater plumes is also thought to cause vertical mixing and enhance melt (MacAyeal, 1984, 1985). Away from the edges of an ice shelf at its center, basal ice is either at equilibrium with the ocean or there is accretion at the ice base. This ice shelf melt pattern is supported by indirect observations of ice shelf melt rates (e.g., Goldberg et al., 2019; Mankoff et al., 2012; Rignot et al., 2013), and melt rates predicted by ocean models (e.g., Goldberg et al., 2019).

Indirect estimates of melt-rate patterns are often derived from remote observations. First, flux divergence is estimated from remote observations and then mass conservation is solved for the basal mass balance. Different approaches to these estimates are outlined in Berger et al. (2017). Such surveys can achieve sub-kilometer scale spatial resolution while covering broad areas. For example, Berger et al. (2017) and Gourmelen et al. (2017) found average melt rates of 0.8 and 7.8 m/a on the Roi Baudouin and Dotson Ice Shelf respectively. At a finer scale, direct observations using radar can resolve basal melt with high accuracy (e.g., Vaňková et al., 2020; Young et al., 2018). Starting with Corr et al. (2002), the Autonomous Phase-sensitive Radio-Echo Sounder (ApRES instrument) has been used to make point measurements of melt rates on ice shelves. Developed by Brennan et al. (2014) and Nicholls et al. (2015), ApRES images the ice base and internal ice reflectors, the latter of which is used to estimate the vertical strain rate profile. Subtracting vertical strain from the change in ice thickness gives a basal melt or accretion estimate (Brennan et al., 2014). High resolution ApRES surveys show large changes in basal melt over small spatial scales (<1 km), particularly near the ice front (e.g., Stewart et al., 2019) and at basal channels (e.g., Dutrieux et al., 2014; Marsh et al., 2016; Stanton et al., 2013).

## 1.2. Basal Channels

On ice shelves in both the Antarctic and Greenland, the surface expressions of long linear channels of relatively thin ice are visible from satellite imagery. For an overview of ice shelf channels in Antarctica see Alley et al. (2016). Ice shelf channels influence the mass budget of ice sheets by redistributing melt patterns. Satellite and ApRES observations have shown increased melt rates within some channels. For example, Marsh et al. (2016) and Stanton et al. (2013) used ApRES to measure melt rates of  $22.2 \pm 0.2$  and 14.2–24.5 m/a in channels on the ice shelves downstream of Whillans Ice Stream and Pine Island Glacier respectively. These studies found that melt rates dropped to near-zero outside the channel between 0.2 and 2 km from the channel apex. Chartrand and Howat (2020) used satellite observations to find similar channel melt rates in the Getz Ice Shelf, estimating melt rates of 22 m/a at the channel apex and near-zero melt rates 2–3 km away. On Pine Island Glacier, Dutrieux et al. (2013) used flux divergence techniques to find that melt in a similar channel was strongest upstream, close to the grounding line. The impact of ice shelf channels on the whole ice shelf is more complex. Both Gladish et al. (2012) and Millgate et al. (2013) used coupled, numerical ice–ocean models to show that when channels focus melt they prevent melting across the rest of the ice shelf. These authors suggested that by reducing melt over the wider ice shelf, these channels might increase the stability of ice shelves, however, their models did not specifically investigate the structural weakening of the ice shelf. Contrarily, observations support the idea that channels have a destabilizing effect on ice shelves (e.g., Alley et al., 2016). Wearing et al. (2021) modeled the role of ice flow in stabilizing ice shelf channels, concluding that in ice thicker than 600 m this flow has a stabilizing effect, but in ice shelves thinner than 400 m this secondary flow is not enough to counteract basal melt. Vaughan et al. (2012) directly observed basal and surface crevasses at a channel, and through numerical modeling found that the stress generated from channel melting could trigger crevasse formation. Meanwhile, Alley et al. (2016) found that basal channels are widely associated with areas of crevassing. Alley et al. (2019) emphasized that the common development of basal channels on the margins of ice shelves increases the susceptibility of ice shelves to rapid break-up or retreat. Rignot et al. (2008) also suggested that the break up of ice shelves, caused by warmer ocean waters, may occur sooner than predicted from the mean reduction in ice shelf thickness due to the intense thinning of ice in basal channels.

Direct access and observations of sub-ice-shelf channels beneath Peterman Glacier in Greenland (Rignot & Steffen, 2008) and Pine Island Glacier in Antarctica (Stanton et al., 2013) have revealed buoyant plumes of meltwater. These meltwater plumes are thought to be strengthened by feedbacks between steep slopes, fast plume flow and enhanced melt rates (e.g., Gladish et al., 2012; Jenkins, 2011; Sergienko, 2013). As plume water melts a sloping ice face, the plume becomes fresher, and more buoyant, and accelerates up the ice face. As the plume accelerates it entrains more water from the surrounding ocean, transporting this relatively warm water to the ice face, further contributing to melting. The melt causes the sloping ice face to steepen, enhancing the melt plume feedback, making pre-existing basal features more pronounced.

Most observations of sub-ice-shelf channels are restricted to their surface expression, in the form of imagery, elevation, and velocity products from satellites. Comparing surface observations with model outputs has provided insights into channel formation. For example, Sergienko (2013) modeled channel formation using a fully coupled ice shelf/ocean model, showing a positive feedback between the basal topography of the ice and a meltwater plume. Their study inferred that high melt rates, and existing variability in ice thickness are required to develop a channel. Satellite observations show that basal channels correspond to areas of high basal melt (e.g., Rignot et al., 2008), and confirm that these channels often originate close to or inside grounding zones (Alley et al., 2016).

While channels are thought to be sustained and deepened by meltwater plumes (e.g., Sergienko, 2013), a variety of mechanisms have been proposed to describe their initial formation (e.g., Alley et al., 2019). Channels can be formed from variability in ice thickness. Alley et al. (2019) used satellite data to show that the lateral shearing at ice shelf margins creates a surface valley that when floated past the grounding line initializes a basal channel. Drews et al. (2017) and Jeofry et al. (2018) used satellite imagery and radio-echo-sounding profiling to show that some channels originate as advection streaks caused by basal topography upstream. Alternatively, Alley et al. (2016) and Le Brocq et al. (2013) identified basal channels co-located with subglacial outflow (as modeled by Le Brocq et al. (2013)), and suggest that subglacial outflow triggers a localized subglacial plume which will form a channel without the requirement of an existing surface valley.

This study aims to further our understanding of subglacially-sourced channel formation. By presenting detailed observations of a basal channel at the grounding line of the Kamb Ice Stream (Figure 1) we aim to better constrain ice and ocean interaction in the channel, and the processes initiating channel formation. This case study of channel formation and growth, is also intended to inform the impact channels have on ice shelf stability. The channel we study here has been noted previously in literature (Alley et al., 2016; Goeller et al., 2015; Horgan et al., 2017; Kim et al., 2016; Le Brocq et al., 2013), and was profiled by the Center for Remote Sensing of Ice Sheets (CREGIS) airborne radar project (Arnold et al., 2020). Because Kamb Ice Stream has little to no ice velocity, this channel is unique as it is not formed by ice advection or shear. As a result, the channel can be used as a natural experiment in plume driven melt processes. Le Brocq et al. (2013), Kim et al. (2016), and Alley et al. (2016) suggested that the channel is formed from submarine melting from a subglacially sourced buoyant freshwater plume.

In the following we use the terms “surface valley” and “basal channel” to distinguish the surface and basal expressions of the channel respectively. “True left” and “true right” are from a perspective looking downstream. Channel “inception” refers to the upstream limit of the basal channel incision. Channel “apex” is the maximum channel height along a lateral transect, while the “walls” are the channels lateral flanks. The “apex” and “walls” run down the length of the basal channel. The surface valley lies at the downstream end of a modeled subglacial drainage path (Figure 1), and optical satellite imagery shows the feature is contiguous with a sinuous feature that cross-cuts streak lines upstream of the grounding zone (Figure 2). Downstream of the channel, the ice shelf exhibits a damaged zone many tens of kilometers long (Figures 1 and 2).

We begin by examining the surface valley of the channel (Section 2.1) using satellite imagery (MODIS MOA (Haran et al., 2014) and LandSat (Roy et al., 2014)) and elevation products (REMA Howat et al. (2019) and ICESat2 Smith et al. (2021)), presenting surface elevation and surface elevation change. In Section 2.2.1 we examine the basal channel underlying the surface valley, using low-frequency (7 MHz) radio-echo-sounding from a series of closely spaced (as little as 250 m) cross-channel profiles. Next, repeat phase sensitive radar (ApRES) observations are used to estimate the basal mass balance within the basal channel in Section 2.2.4. We then discuss the implications of these results, first constraining the mechanism that creates the channel (Section 4.1), and explaining why we see discrepancies between the ice base and surface observations (Section 4.2). We then estimate a lower bound on the melt rate magnitude in the basal channel (Section 4.3). Last, we discuss processes

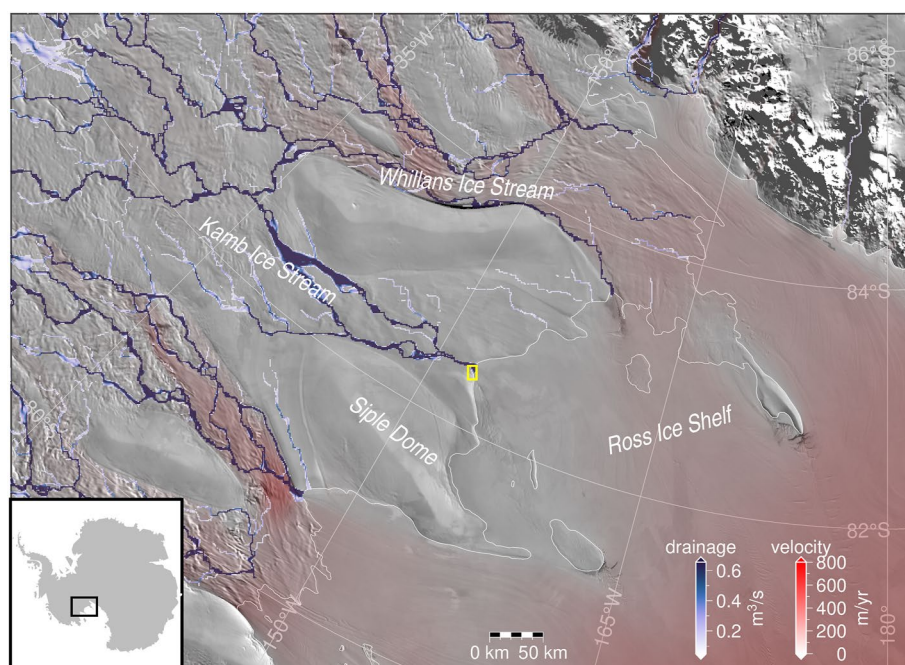


**Figure 1.** Map showing the Siple Coast region. The study area is plotted as a yellow box at the grounding zone of the Kamb Ice Stream. Figures 3, 5, and 6 cover this study area. Modeled subglacial drainage of the Siple Coast is in blue (Le Brocq et al., 2009), grounding line and coastline (Depoorter et al., 2013) are plotted as thin white lines. Background image is MODIS MOA 2009 (Haran et al., 2014) overlaid with MEaSUREs Phase-based Ice Velocity (Mouginot et al., 2019). Antarctic place names are labeled in white. Figure produced using PyGMT (Uieda et al., 2021; Wessel et al., 2019) with scientific color maps (Crameri, 2018). Plotted using an Antarctic Stereographic Projection with a standard latitude of 71°S (EPSG:3031).

that could explain our observations. In particular, the linear shape of the channel (Section 4.4.1), the steep shape of the channel inception (Section 4.4.2), and ledges in the channel (Section 4.4.3).

### 1.3. Kamb Ice Stream

Kamb Ice Stream once drained from the interior of the West Antarctic Ice Sheet into the Ross Ice Shelf, flowing at speeds greater than 350 m/a (Ng & Conway, 2004). Around 150 years ago, it stagnated to a speed of around 10 m/a (Ng & Conway, 2004; Retzlaff & Bentley, 1993). As a result of this change in flow, Kamb Ice Stream is often referenced as an example of internal variability in ice stream flow (e.g., Hulbe & Fahnestock, 2004). The grounding line of the Kamb ice stream is thought to have occupied its current position in the last  $\approx 150$  years, prior to which it was downstream (Fried et al., 2014). Horgan et al. (2017) suggest that the grounding line likely retreated to its current location in a stepwise manner after the ice stream's stagnation. If the Kamb Ice Stream reactivated, ice discharge from West Antarctica would potentially increase by 20 Gt/a (Jacobel et al., 2009). While the variability in the flow of the Kamb Ice Stream is often attributed to changes in subglacial drainage, there is no clear evidence of how this happened. The leading hypothesis proposes that water was rerouted away from the ice stream, increasing the resistance to ice flow at the ice base (e.g., Anandakrishnan & Alley, 1997), though observations still indicate ample water at the base of the ice stream (Engelhardt & Kamb, 1997).

## 2. Methods

To estimate ice surface elevation and ice thickness in the study area we used a collection of remote sensing products and over-snow radio-echo-sounding. Basal mass balance is estimated at point locations using repeat ApRES. Data coverage is shown in Figure 3. This section outlines the remote sensing products used and describes the ApRES and radio-echo-sounding processing along with the interpolation methods used to estimate ice thickness and ice base topography.



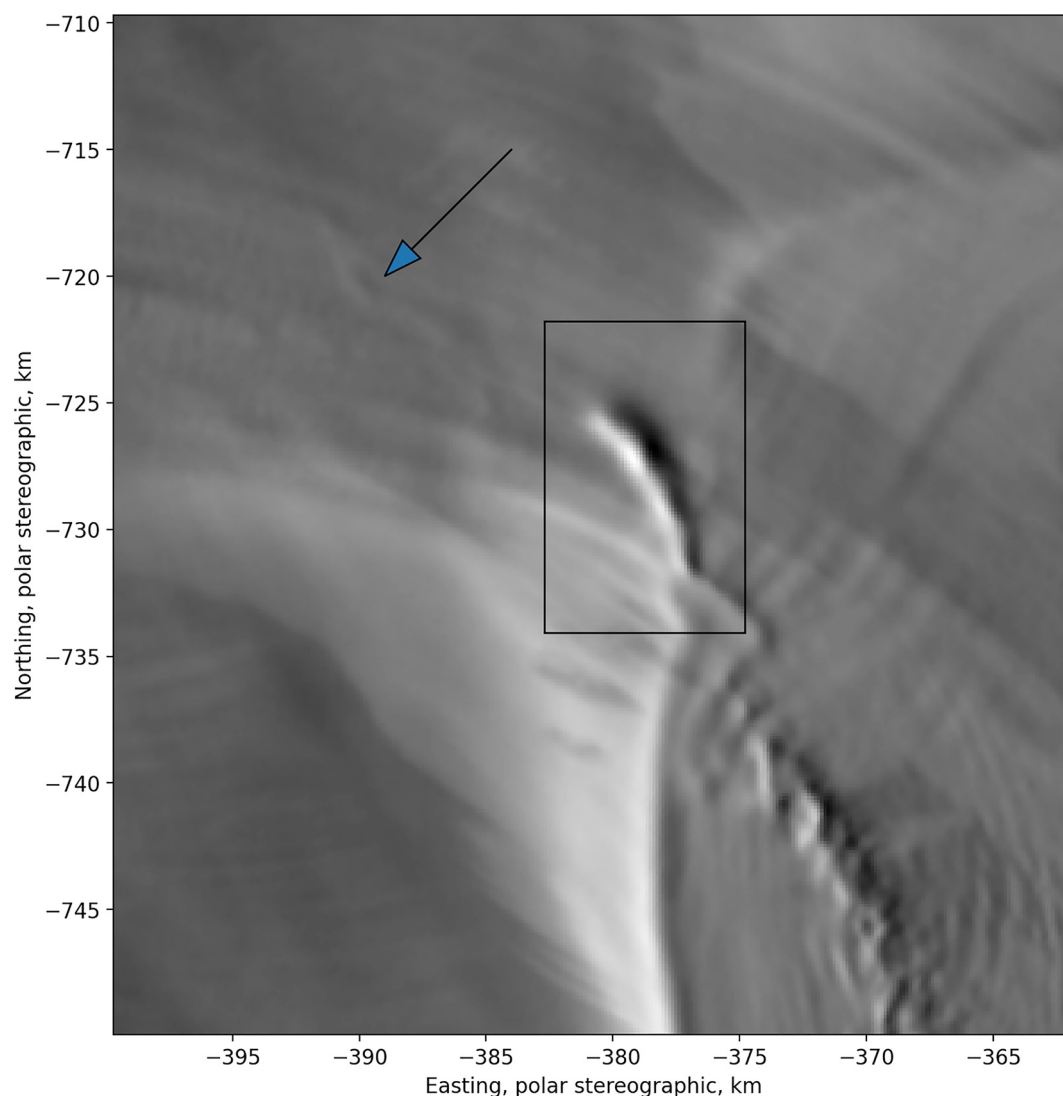


**Figure 2.** MODIS MOA (2009) imagery of wider study area (Haran et al., 2014). Arrow points to possible continuation of the surface valley upstream of the main study region. Black box outlines the study area shown in Figures 3, 5, and 6.

## 2.1. Surface Elevation and Morphology

Four different remote sensing products were used to study the surface valley (Table 1). Optical satellite imagery included Landsat 4–8 (Roy et al., 2014) and the 2009 MODIS Mosaic of Antarctica (MOA) (Haran et al., 2014). Landsat 4, 5, 7, and 8 showed temporal change in the surface valley, and showed the earliest image of the valley in 1985. The 125 m spatial resolution MODIS MOA product provided a broader view of the study area and surrounding surface. For surface elevations, we used ICESat–2 and Reference Elevation Model of Antarctica (REMA) strips (Howat et al., 2019; Smith et al., 2021). ICESat–2 track coverage is shown in Figure 3. We debiased the REMA strips using swath-processed CryoSat–2 data (Gourmelen et al., 2018).

REMA strips provided the most detailed view of surface elevation, with 2 m pixels over the study area. While nine strips from December 2012 to September 2017 pass over the study area, most have some cloud cover or miss a significant portion of the study area. The REMA strip from 9 November 2016 has full coverage, so was used to calculate ice base elevation from radar-derived ice thickness. A second REMA strip from 24 December 2012 was differenced from the 2016 strip to calculate the temporal gradient in the ice surface. The 2012 and 2016 REMA strips state a vertical accuracy of 4 and 3.5 m respectively (Howat et al., 2019; Noh & Howat, 2015). However, the elevation models are expected to be more accurate over the study area which is relatively stable due to low surface

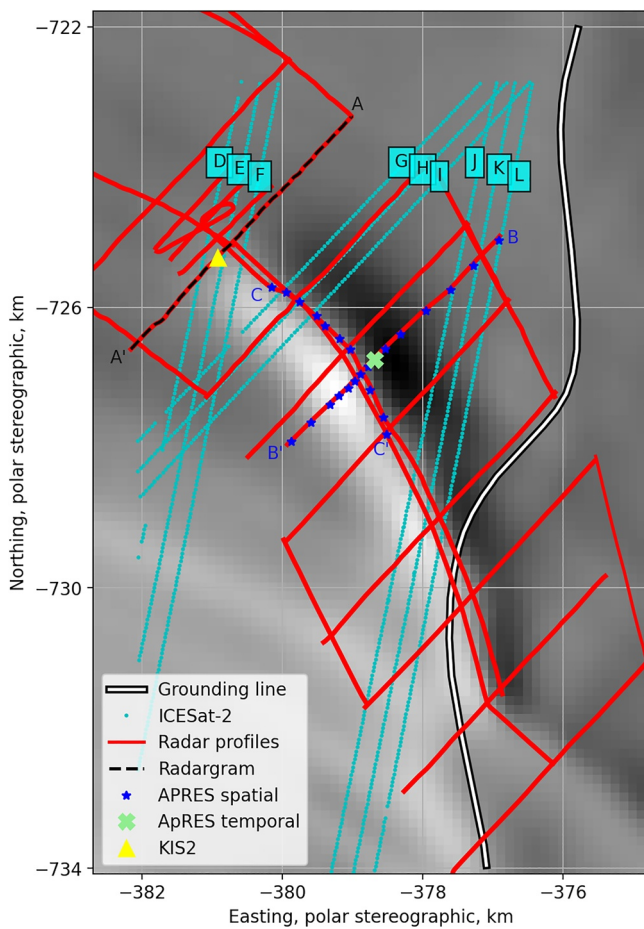


**Figure 3.** Map of study area showing location of data. Ice flow direction is from top left to bottom right. Background image is MODIS MOA 2009 (Haran et al., 2014). Red lines are low-frequency radar profiles, white line is grounding line from Depoorter et al. (2013), black dashed line shows location of radar profile in Figure S2 in Supporting Information S1, blue stars are autonomous phase-sensitive radio-echo sounder (ApRES) repeat measurement locations, and light blue dots are ICESat-2 tracks. ApRES was placed continuously recording at the light green “X,” and the yellow triangle marks the planned location of a direct access drilling site scheduled for drilling in late 2021. Letters A–L are referred to in subsequent figures.

velocity (Rignot et al., 2017). Prior to differencing REMA strips we first bias corrected the REMA data using elevation data generated using swath processing of CryoSat data by Gourmelen et al. (2018). (Monthly swath point data available from ESA CryoTEMPO project: <https://cryotempo-eolis.org/>). We bias corrected by calculating the mean difference between masked REMA strips and contemporaneous masked CryoSat-2 data, with the mask omitting the floating ice shelf and channel feature. The mean differences (−2.00 and −3.91 m for 2012 and 2016 CryoSat-2 minus REMA respectively) were then added to the REMA strips prior to differencing to create Figure 5d. We also tested calculating and removing a best-fitting plane to the CryoSat-2 minus REMA differences but this resulted in less satisfactory results, with an unrealistic gradient in elevation change across the margin of the ice stream.

We used ICESat-2 ATL11 point elevations (Smith et al., 2021), which had nine tracks crossing the study area. The reference ground track numbers for these tracks are 114, 175, 349, 410, 617, 852, 1,059, 1,120, 1,294. These were acquired more recently (since 2019) than the REMA elevation strips. Mean surface measurement precision from ATL11 points over the study area was 1.12 cm (Figure S1 in Supporting Information S1). For ICESat-2 differences a year apart, we double this mean surface precision to get an uncertainty of 0.02 m/a. All elevations in this paper are referenced to the GL04C geoid datum, which is approximately 47 m below the WGS84 ellipsoid datum in the study area. Elevation differences from ICESat-2 ATL11 point elevations were also compared to differences calculated using debiased REMA strips.

## 2.2. Ice Thickness

### 2.2.1. Low Frequency Radar

To estimate ice thicknesses over the channel, the study area was profiled using low-frequency (7 MHz) radio-echo-sounding. Radar profiles were 1,000–1,400 m apart, except at the head of the channel where the spacing between lines was reduced to approximately 200 m to better constrain the inception of the channel (Figure 3). Data collection followed Christianson et al. (2016). The radar transmitter and receiver were towed on sleds at approximately 8 km/hr resulting in an average spatial resolution along radar lines of 1.8 m. Data processing included dewowing, bandpass filter (1–2–15–18) MHz, along track spatial stacking into 3 m bins, and debiasing. The data were then finite difference migrated at 169 m/μs, before a final (3–4–15–18) MHz bandpass filter was applied. The resulting profile data include off-nadir reflections (discussed in more detail in Christianson et al. (2016)), which

are difficult to interpret but must be considered during analysis. Radar survey positioning used Global Navigation Satellite Signal (GNSS) observations, post processed using the Precise Point Positioning kinematic method (Natural Resources Canada, 2016). An example processed radar line is shown in Figure S2 in Supporting Information S1. The location of all radar lines are shown in Figure 3. Following Dowdeswell and Evans (2004), a firm correction of +7 m was added to ice thickness. Additionally, +7 m was added to ice thickness to correct the

**Table 1**  
Remote Sensing Products Used in This Study

Products	Data timespan	Site coverage	References
REMA 2m strip	12/2012–09/2017	2 m pixels of site area	Howat et al. (2019)
ICESat-2	4/2019–Ongoing	6 tracks across channel	Smith et al. (2021)
Landsat	1985–Ongoing	20 m pixels covering site area	Roy et al. (2014)
MODIS MOA	–	125 m pixels covering site area	Haran et al. (2014)

offset between the low frequency radar and the more accurate ApRES ice thicknesses. This difference is likely caused by the low frequency radar trigger threshold and was calculated using the mean difference between ice thicknesses derived from coincident ApRES and low frequency radar at line BB' shown on Figure 3.

### 2.2.2. Ice Base DEM

We estimated the three dimensional shape of the basal channel by digitizing the base of the ice and then interpolating between radar profiles. Our observations of ice thickness had high spatial sampling across the channel (3 m trace spacing) and low spatial sampling in the downstream direction (profile spacing of 200–1,400 m). This meant that conventional interpolation techniques failed to capture the shape of the steep sided narrow channel (Figure S3 in Supporting Information S1). To overcome this we use an interpolation method that is based on the assumptions that the channel is bounded laterally and has downstream continuity. First, all radar lines crossing the channel were resampled spatially from the channel apex to either side of the channel. Equivalent points from each line were then interpolated downstream with a cubic spline. These along-channel interpolated profiles were then interpolated altogether onto a regular grid with 2 m spacing. Because radar lines parallel to the channel included some off-nadir reflections that were not correctly repositioned by two-dimensional migration, they were not used in the interpolation. Ice thickness in the study area not over the channel was estimated using linear interpolation of all radar line points outside the channel. The channel thickness interpolation was cropped onto the surrounding ice thickness estimate, and the whole study area was again gridded using a nearest-neighbor interpolation. The resulting estimate of ice thickness (Figure S4 in Supporting Information S1) was then subtracted from a debiased 2 m REMA surface elevation strip to produce ice-base elevation (Figure 5c). The resulting interpolation of the basal channel shape was verified through comparisons to independent basal elevation estimations provided by CReSIS (Arnold et al., 2020), which had three lines passing over the basal channel in the study area.

One goal of estimating an accurate channel shape is to better constrain the freshwater plume within the channel. For this, the gradient of the channel inception is important, as it is a dominant forcing in plume melt rate models (Jenkins, 1991). Locating the inception of the channel, however, is not straightforward due to off nadir reflections. The channel inception is best imaged by a radar line parallel to channel direction (Figure S5 in Supporting Information S1). From this, we deduce that the farthest upstream radar line which has a reflection crossing the channel, shows an off nadir reflection. This interpretation is confirmed by the fact that this radar profile indicates a reflection distance equal to the distance to the channel reflection on the next radar line. In the channel interpolation, the channel depth is set to be zero at this off nadir reflection, which constrains the downstream distance or angle over which the channel forms.

### 2.2.3. Hydrostatic Equilibrium

For each pixel from the ice base DEM, we calculated the vertical distance which the ice column is offset from hydrostatic equilibrium. An offset of zero describes ice at hydrostatic equilibrium, and a negative/positive offset indicate the ice column is held below/above equilibrium by external forces. To calculate this measure we first estimated average density of the ice column for each pixel, using ice thickness from the interpolated DEM (Section 2.2.2) and the density-depth model of Herron and Langway (1980). For the density model, we assumed an accumulation rate of 0.1 m/a (Lenaerts et al., 2012), a mean annual temperature of  $-27.3^{\circ}\text{C}$ , and initial, critical and ice densities of 300, 555, and  $917\text{ kg/m}^3$  respectively. Next, using Archimedes principle, ice thickness and average density, we calculated the theoretical freeboard if the ice column at each pixel were at hydrostatic equilibrium. This is calculated as  $h_{\text{freeboard}} = h_{\text{thickness}} (1 - \bar{\rho}_i / \rho_s)$  where  $h_{\text{freeboard}}$  is the freeboard elevation of the pixel at hydrostatic equilibrium,  $\bar{\rho}_i$  is the average density of the ice column for a pixel and  $\rho_s$  is the density of displaced seawater which we set to  $1,030\text{ kg/m}^3$ . We subtracted the resulting freeboard elevation from the debiased REMA elevation of the region corrected to the GL04 geoid to get the vertical offset from floatation (Figure 7).

### 2.2.4. ApRES

Basal mass balance was surveyed using ApRES on two profiles, one parallel to the surface valley low, the other crossing the channel (Figure 3). ApRES observations were made in December 2019 and repeated in December 2020 at the same locations, which we marked with flags. The ApRES antennae had a parallel orientation and were spaced 9 m apart. Data collection and processing followed the method described in Stewart et al. (2019). The ApRES surveys are not migrated so results may show off nadir reflections. While the ApRES can observe accretion, quantifying the rate is problematic due to the occurrence of multiple reflections from both the glacial/marine–

ice interface and the marine–ice/water interface, and unknown changes in the properties of marine–ice (Vaňková et al., 2021). The values presented should be interpreted as an “apparent accretion” rate as described by Vaňková et al. (2021).

### 3. Results

#### 3.1. Topography

##### 3.1.1. Surface Topography

The surface valley is visible in the first available imagery from Landsat 5 in 1985 and extends further upstream in subsequent Landsat imagery in 1989, 2002, and 2020 (Figure 4). While changing illumination angles may affect the apparent migration of the valley, the apparent migration appears to exceed any direct shading effects. By 2020 the channel appears more defined and extends approximately 1.5 km upstream of the 1985 surface channel. The 2016 REMA strip shows that the surface valley was approximately 2 km wide, over 10 km long and had a maximum depth of 15 m relative to the adjacent ice stream (Figure 5b). The valley starts abruptly, 5 km inland from the Depoorter et al. (2013) grounding line (Figure 3). The surface gradient at the head of the valley is approximately  $-1^\circ$ , then the valley is fairly straight and flat-bottomed for around 1.5 km. The valley then exhibits three distinct but connected basins downstream (labeled B1, B2, B3 in Figures 4 and 6) corresponding to bends in the basal channel. Both the surface valley and basal channel first turn to the true right by  $30^\circ$  (B1), then right by  $20^\circ$  (B2) then left by  $60^\circ$  (B3) at the three basins respectively. On the surface, high points between basins are 3–7 m higher than the basin lows, and the valley is 5%–10% wider at the basins. In historic imagery (1985, 1989; see Figure 4) the three basins are visible, and the surface valley does not extend upstream from the three basins. In the 2009 MODIS MOA imagery, a faint trace of the surface valley continues upstream from its clear head for 10 more kilometers (Figure 2 and Figure S6 in Supporting Information S1). The faint trace of the surface valley upstream does not correspond to a basal channel large enough to be visible in radar profiles. Additionally, the channel continues downstream from the study area shown in Figure 5c, though surface imagery shown in Figure 2 suggests that out of the study area, the basal channel is less pronounced.

##### 3.1.2. Ice Base Topography

The downstream profile of the channel apex is best imaged by radar lines perpendicular to the channel. Radar lines following the channel do not accurately show channel depth due to off nadir reflections. The bisection of perpendicular radar lines and the channel apex are shown in Figure 6 as “Surveyed channel apex” and are interpolated to produce the “Interpolated channel maximum” as described in Section 2.2.2. The “Surveyed channel apex” show the basal channel starts abruptly, approximately 300 m upstream from the start of the surface valley (Figure 6b). The inception of the basal channel inclines from 0 to 300 m above the bed over less than 300 m horizontally, constrained by the spacing between parallel radar profiles. Therefore, the initial gradient of the basal channel is constrained as between  $45^\circ$  and  $90^\circ$  from horizontal. Over 500 m downstream the basal channel incises approximately 50% of ice thickness (350 m of 700 m), to a maximum elevation of  $-325$  m (Figure 6a). The “Surveyed channel apex” then shows a reduction in basal channel height of greater than 30 m to an elevation of  $-330$  m at 0.75 km downstream from its inception (Figure 6a). Interpolating between data points, we estimate that the channel apex (“Interpolated channel maximum”) has a local minimum 1.25 km in the downstream direction at  $-390$  m elevation. Downstream the surveyed channel apex then indicate that the basal channel apex rises to around  $-340$  m at 3.5 km then lowers to around  $-380$  m at 10 km (Figure 6a) at the edge of the study area. Past 10 km, the channel has not been surveyed. The elevation of the surface valley is at approximately 80 m (Figure 6b).

The basal channel has three bends which correspond to surface basins B1–B3 (described in Section 3.1.1). The channel is around 200 m wide for almost 1 km from its inception, then widens to 700 m at the first bend (B1) 3.9 km down the channel, narrows to 450 m then widens to 1,050 m at the bend (B2) 6.4 km downstream (Figure 6 and Figures S7 and S8 in Supporting Information S1). These widths are measured at radar lines and are therefore not a result of interpolation. While there are no radar lines crossing the channel at the third bend (B3), the interpolation estimates that the basal channel narrows to 200 m and widens to 600 m at the third bend (B3) 8.5 km downstream (Figure 5c and S7 in Supporting Information S1). While these bends correspond to basins in the surface elevation, they do not correspond discernibly to changes in the ice base elevation.



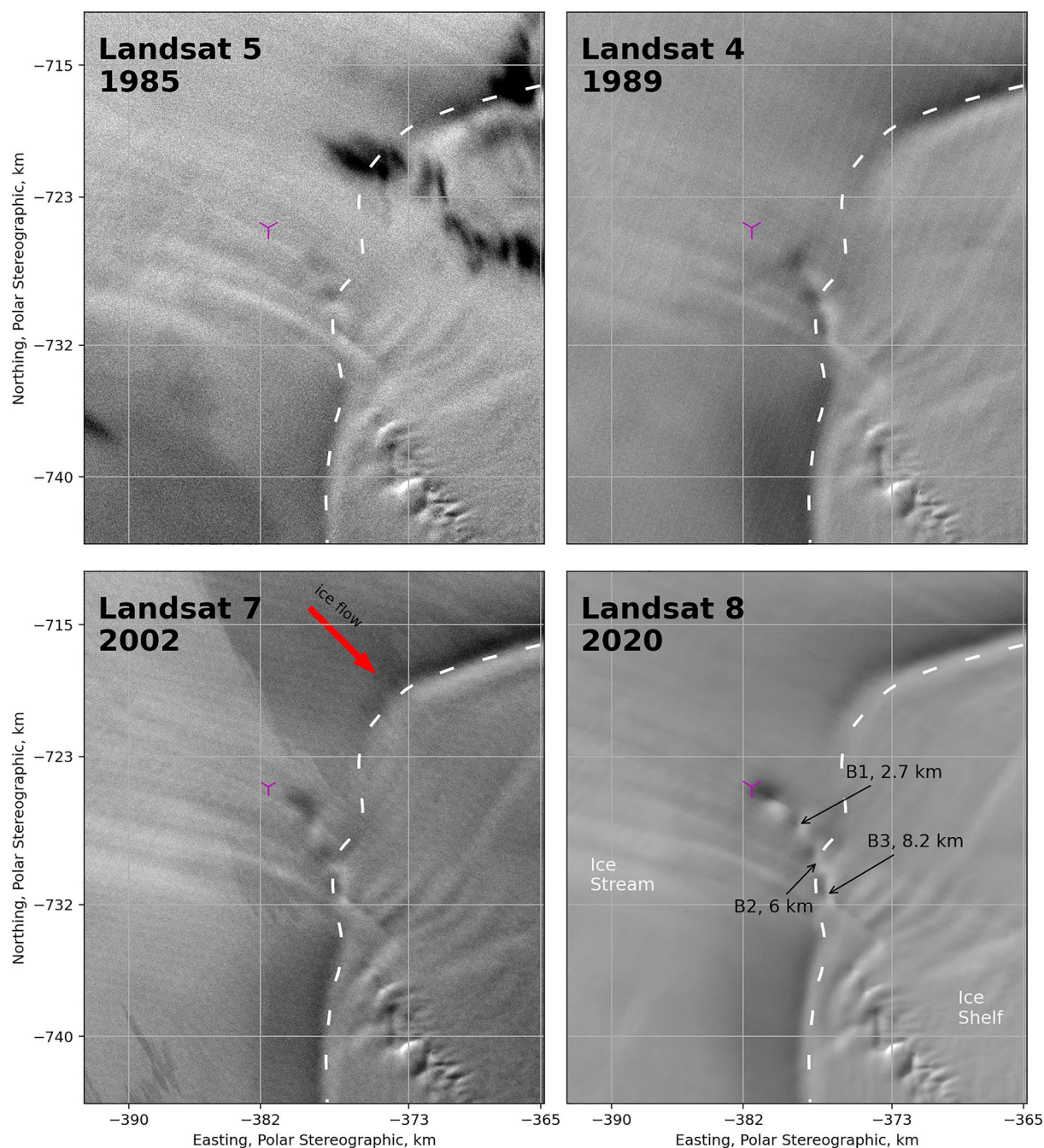


**Figure 4.** Landsat imagery of a visible valley in the ice surface (Roy et al., 2014), shown in the central grid square at  $(-380, -725)$  km. The surface valley sits at the outlet of estimated subglacial drainage paths (Figure 1), and is the surface expression of a sub-ice-shelf channel. Purple “Y”s are an arbitrary reference point. The grounding line (Depoorter et al., 2013) is shown as a white dashed line, which divides the Kamb Ice Stream and the Ross Ice Shelf. Red line shows direction of ice flow. Basins B1–B3 are topographic lows in the ice surface, distances are from the upstream start of the interpolated channel maximum to each basin center.

The cross-sectional shape of the basal channel varies along flow. While the basal channel flanks are imaged to be consistently vertical, the channel has distinct ledges along its sides (Figures S8 and S9 in Supporting Information S1). These ledges are separated from the apex of the basal channel by a vertical offset. For around 1 km downstream of the basal channel inception, a ledge is visible on the true left (L1; Figures S8 and S9 in Supporting Information S1), this is separated from the basal channel apex by a wall ranging from 200 m at first to 50 m further downstream. A ledge on the true right is then apparent from around 1–6 km downstream from the channel inception (L2; Figures S8 and S9 in Supporting Information S1). This ledge is widest at the bend (B1) 3.9 km

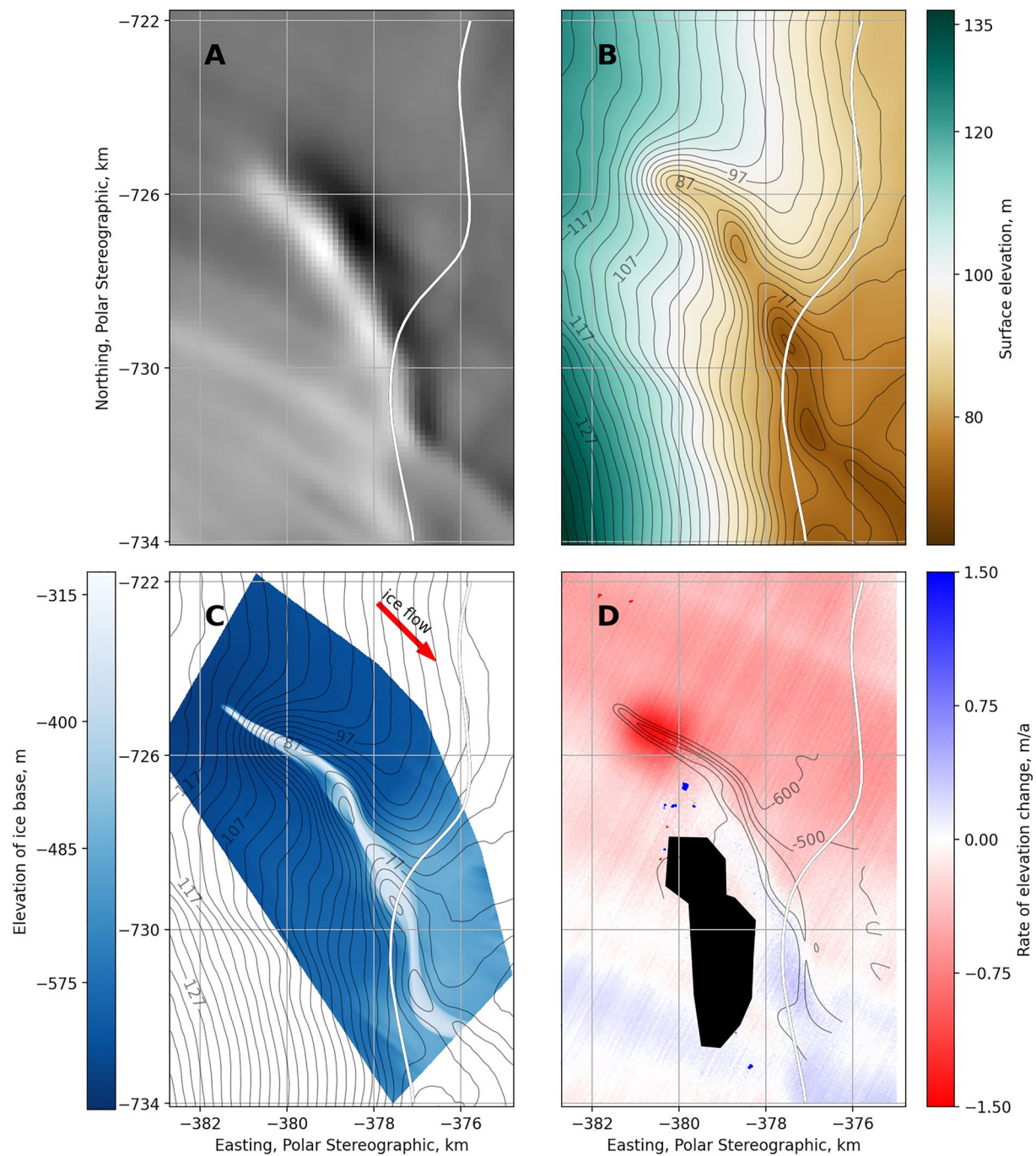


**Figure 5.** (a) MODIS MOA (2009) optical image of study area (Haran et al., 2014). (b) Reference elevation model of Antarctica (REMA) ice elevation, 2 m resolution (Howat et al., 2019). The white line is the grounding line from Depoorter et al. (2013) (c) Estimated channel ice base elevation interpolated from radar survey, contours of REMA surface elevation. Red arrow shows direction of ice flow. (d) Difference between REMA elevation from 24 December 2012 to 9 November 2016, contours show estimated ice base. Black area is masked out due to clouds.

downstream from the channel inception at which point the ledge is 150 m below than the channel apex. A third ledge (L3; Figures S8 and S9 in Supporting Information S1) is visible from 4 to 6.6 km downstream from the channel inception. The last 4 km of the channel has no observable flat ledges and the channel walls appear to have a gentler slope than those upstream.



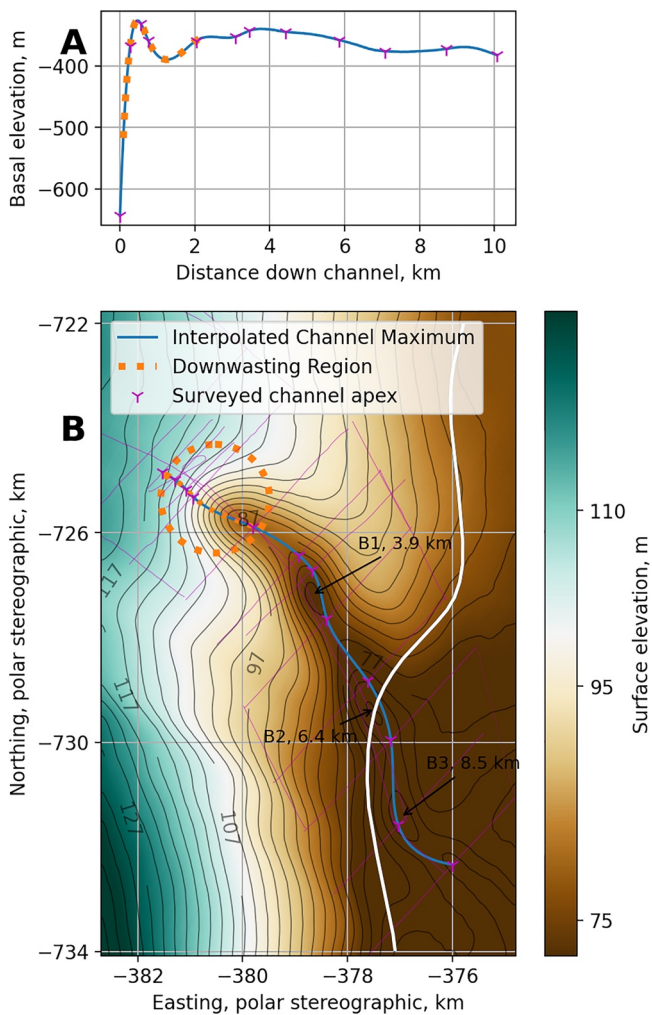


**Figure 6.** (a) Estimated ice base elevation along the apex of the channel, calculated by interpolating between the maximum height of each radar line crossing the channel (“Surveyed channel apex”). (b) Estimated channel apex position plotted over Reference elevation model of Antarctica (REMA) surface elevation. Basins B1–B3 are topographic lows in the ice surface, distances are from the upstream start of the Interpolated channel maximum to each basin center. The region of surface lowering is delineated by orange dotted region, and coincides with the onset of the surface valley. White line is the grounding line from Depoorter et al. (2013).

### 3.1.3. Hydrostatic Equilibrium

The basal channel inception appears approximately 6 km upstream of the grounding line estimated by Depoorter et al. (2013). The vertical offset of the ice column from hydrostatic equilibrium indicates where the ice is freely floating and ranges from  $-10$  to  $45$  m over the study area (Figure 7). A positive vertical offset denotes an ice column which is held above floatation, either by the ground or from internal ice stresses. A vertical offset of zero denotes ice which is floating, and a negative vertical offset denotes an ice column held beneath hydrostatic equilibrium by lateral ice stresses. Upstream of the surface valley, the vertical offset of the ice from equilibrium is positive  $20$  m, showing that the ice is well grounded. Outside the surface valley, the vertical offset decreases steadily downstream. By  $8$  km downstream from the channel inception, the ice outside of the surface valley is at hydrostatic equilibrium. The ice column directly over the basal channel has positive vertical offset from floatation, peaking at  $45$  m above floatation at the upstream end of the basal channel and dropping to  $10$  m above floatation at the downstream end of basal channel within the study area. Along the length of the channel, the channel apex is offset further above the floatation height than the sides, which are  $10$ – $20$  m closer to floatation. In areas under the surface valley but not above the sides of the basal channel, the ice column is offset below floatation by up to  $10$  m. This occurs along the length of the surface valley, and is especially pronounced on the true right.

## 3.2. Change in Topography

### 3.2.1. Change in Surface Topography

Near the inception of the basal channel, a region of modern surface lowering is apparent when differencing bias corrected (see Section 2) REMA elevation strips from 24 December 2012 and 9 November 2016 (Figure 5d). We estimate an uncertainty for our REMA strip differences from the interdecile range (1st–99th) of the values outside of the channel (Figures S11 and S12 in Supporting Information S1). This conservative method results in an uncertainty of  $\pm 0.4$  m/a. The region of surface lowering is a circle with a radius of approximately  $1.0$  km. This region is centered near the onset of the surface valley (Figure 6b) with the start of the basal channel located at the upstream margin of the region of surface lowering (Figure 6). The region of greatest surface lowering is centered approximately  $1$  km downstream from the onset of the basal channel (Figures 5c and 5d). This region has a maximum of  $-1.8 \pm 0.4$  m/a at its center, and has a mean elevation change of  $-0.9 \pm 0.4$  m/a (Figure 5d).

Differences from ICESat-2 point elevations from 9 May 2019 to 5 August 2020 show the same pattern, with surface lowering up to  $-1.25 \pm 0.02$  m/a

on three upstream lines that cross the circular region (Figures 8d–8f). One kilometer downstream from this region, ICESat-2 point elevations show more complex changes in surface elevation (Figures 8g–8i): while the background ice stream's surface is lowering at around  $-0.2 \pm 0.02$  m/a, the surface valley's sides are lowering more quickly, with the true right side lowering up to  $-0.4 \pm 0.02$  m/a more than the background ice stream (Figures 8g–8i). This suggests that the channel is widening, but not deepening in this area. Further downstream, the REMA strip difference shows an increase in surface elevation along the true right side of the valley shown in Figure 5d between  $(-379.5 \text{ km}, -727 \text{ km})$  and  $(-377.5 \text{ km}, -730 \text{ km})$ . While the REMA difference signal does not exceed the uncertainty, the more accurate ICESat-2 differences confirm these elevation changes. At the downstream end of this area (coincident with the basin B2 labeled in Figure 6), the ICESat-2 differences from 2019 to 2020 (Figures 8j–8l) show up to  $0.1 \pm 0.02$  m/a of increase in surface elevation on the true right of the valley and  $-0.3 \pm 0.02$  m/a of lowering on the true left, suggesting that the valley is migrating to the true

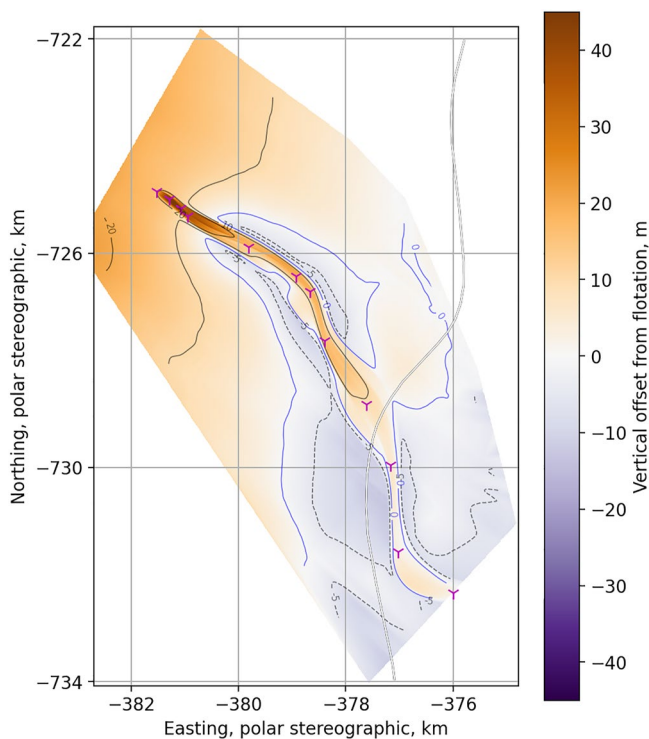


**Figure 7.** Vertical offset from hydrostatic equilibrium, calculated from reference elevation model of Antarctica ice surface (Howat et al., 2019), and ice base interpolation (Figure 5). Blue line indicates the zero contour, where ice is estimated to be floating. Positive values indicate ice is held above flotation either by the ground, or by bridging stresses with surrounding ice. Negative values indicate ice is held below flotation by lateral stresses with surrounding ice. White line is the grounding line from Depoorter et al. (2013). Magenta markers denote “Surveyed channel apex” as in Figure 6.

left. Background surface lowering on ICESat-2 lines J, K, and L is between  $-0.1 \pm 0.02$  and  $-0.2 \pm 0.02$  m/a (Figures 8j–8l). This location is coincident with the location of ledge L2 (Figures S8 and S9 in Supporting Information S1) discussed in Section 3.1.2.

### 3.2.2. Change in Ice Base Topography

While caution should be taken when interpreting accretion rate estimates from repeat ApRES observations, our observations indicate accretion is occurring within the downstream portion of the basal channel (Figure 9). On the cross channel profile (see Figure 3 for the location), all but one of the ApRES survey sites outside the channel indicate basal melt. In the channel, all sites indicate apparent accretion. Apparent accretion peaks on the true right of the channel, coincident with a ledge (L2; Figures S8 and S9 in Supporting Information S1) and surface raising detected by REMA strip differencing (Figure 5d and Sections 3.1.2 and 3.2.1). ICESat-2 data also show surface raising on the channel right in a similar area (Figure 8). Vertical strain rates derived from ApRES observations map roughly to melt rates (Figure 9). Strain is most negative where accretion is strongest, and low melt rates map to sites with low strain. Two sites at the channel apex are an exception, where accretion is strong and strain is close to zero.

## 4. Discussion

We have presented a detailed examination of an sub-ice-shelf channel, providing observations which constrain theories of ice and ocean interaction in the channel, and processes which have formed the channel. We next discuss how the observations presented, such as the surface lowering and channel shape, can constrain theories of plume migration, plume processes and provide bounds on melt rates. We discuss the mechanism which caused the formation of the channel, the impact of bridging of ice stresses on observations, constraints on basal melt rates based on surface observations, and the implications of the channel shape on channel processes.

### 4.1. Channel Source

Our observations confirm that the surface valley described in Section 3.1 is the expression of a basal channel as concluded by Le Brocq et al. (2013), Kim et al. (2016), and Alley et al. (2016) (Figure 5c). As the channel's location corresponds to predictions of concentrated subglacial flow (Figure 1), it is most likely that the channel has been incised by a subglacially sourced meltwater plume. Under Kamb Ice Stream, subglacial meltwater has been modeled as concentrating in a single hydropotential low before flowing to the sea (Carter & Fricker, 2012; Le Brocq et al., 2013). When this freshwater meets the salty ocean it likely forms a buoyant plume which entrains warmer ocean water (as described by Sergienko (2013)), and incises the channel into the underside of the Ross Ice Shelf (Figure 5). Plume driven melt likely incises the channel both higher into the ice and upstream following the subglacial drainage route. As the channel grows, the grounding line is shifted locally upstream, and salty bottom water flows upstream to replace fresh plume driven outflow in the top of the water column (Figure 7). The resulting shape and circulation is likely comparable to an estuarine river mouth, whereby the sea and freshwater meet in a channel which forms a local deviation from the coastline. In addition to a classic estuary, a meltwater plume at the inception of the channel directly couples fresh and salty layers by entraining the upstream flow of salty bottom water and expelling buoyant fresh water.

We interpret the surface lowering (Figure 5d) as caused by submarine melt and subsequent adjustment of the ice toward hydrostatic equilibrium. The region is approximately  $3.7 \text{ km}^2$  and the surface is lowering at an average rate of  $-0.9 \pm 0.4 \text{ m/a}$ . Subglacial melting is likely occurring, or occurred, over an elongated region of the channel, though the surface expression does not directly reflect the shape of the ice base. We attribute the general mismatch of surface and basal topography to bridging stresses in the ice.



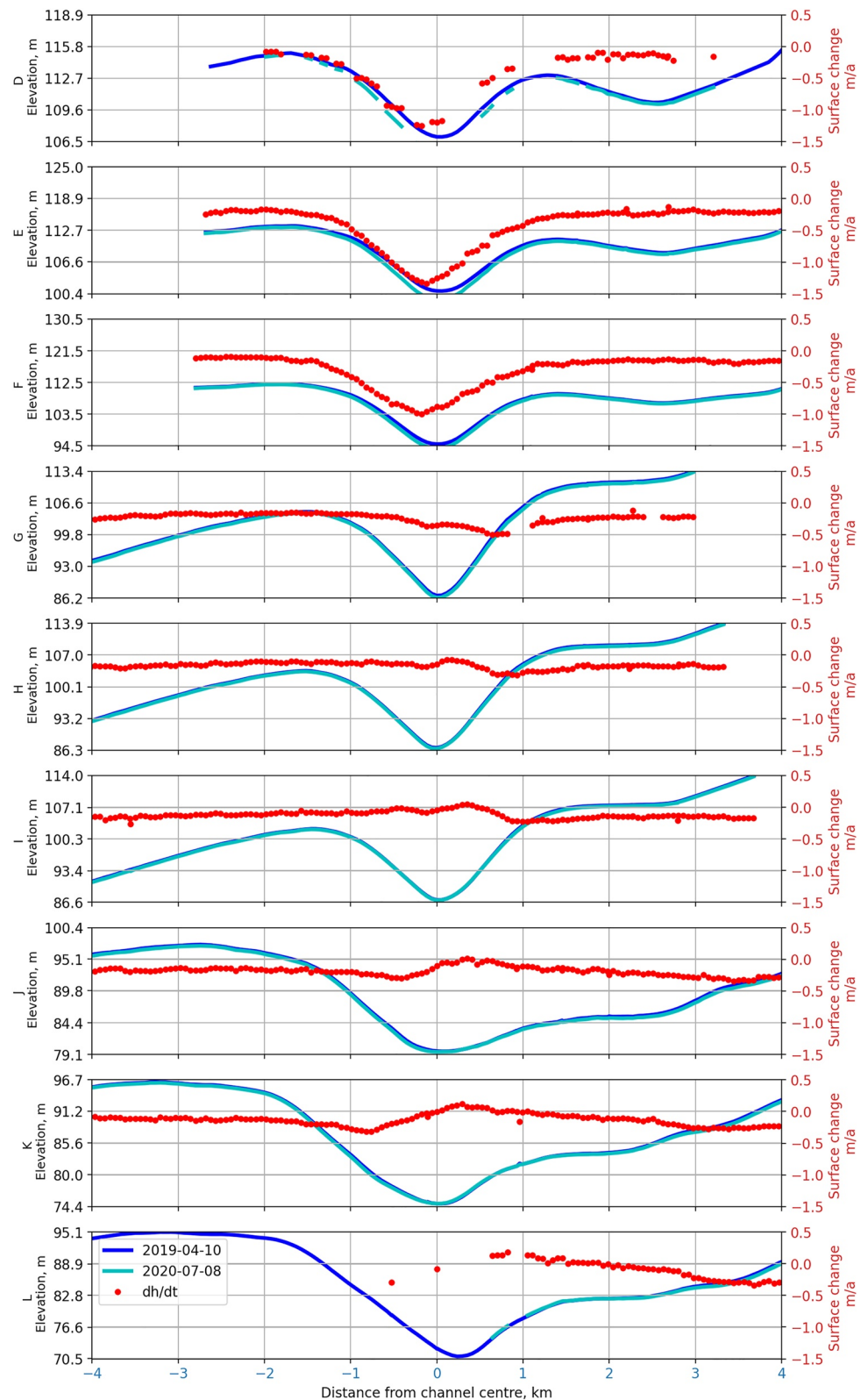


**Figure 8.** ICESat-2 along track elevations and differences for nine tracks which cross the surface valley in 2019 and 2020. Locations of the lines are shown in Figure 3 and Figure S10 in Supporting Information S1. Lines D to L are in order from upstream to downstream. Lines are shown looking downstream, positive distance from channel center corresponds to true right.

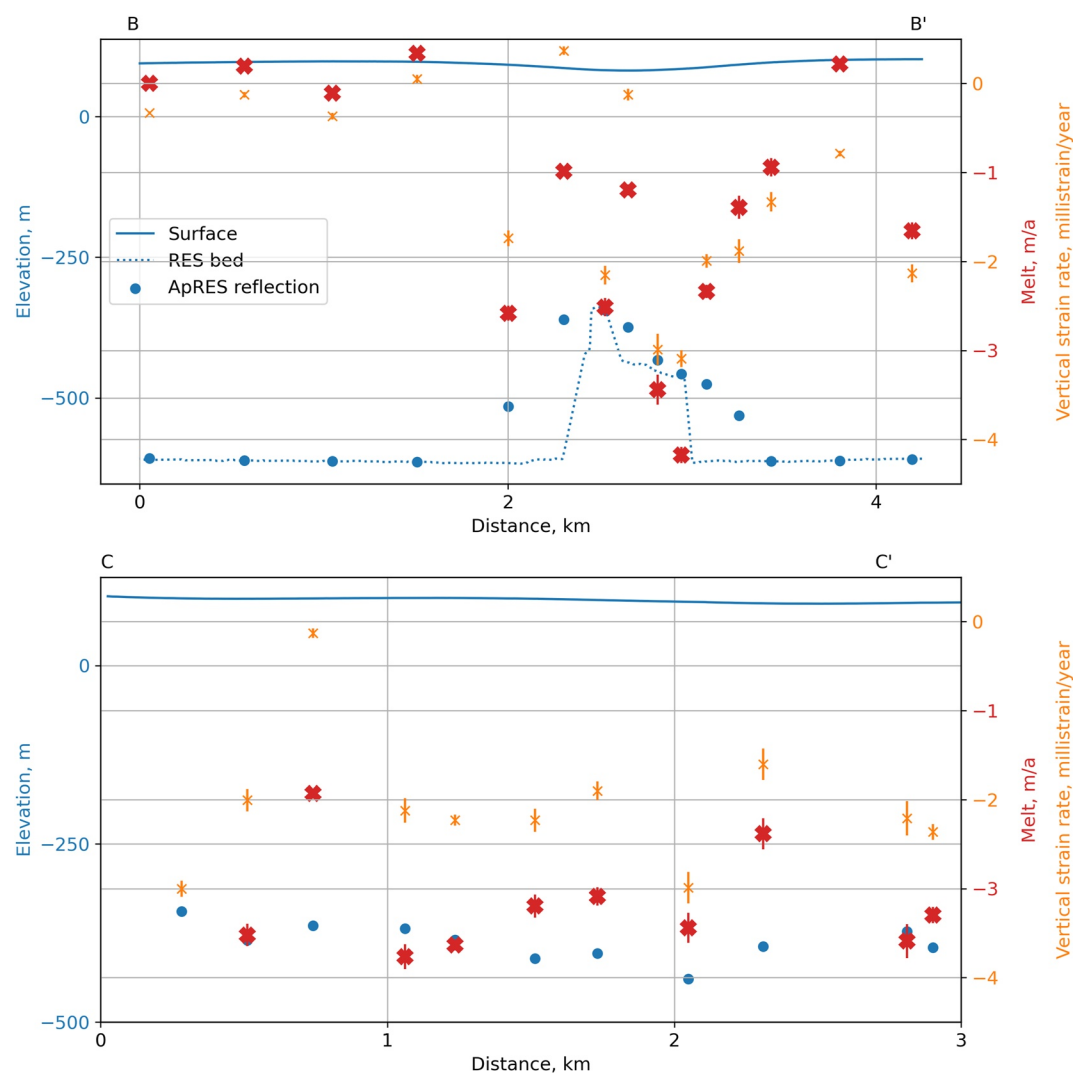


**Figure 9.** Autonomous phase-sensitive radio-echo sounder (ApRES) basal mass balance on two profiles the channel shown in (Figure 3). “B” crosses the channel at right angles, “C” follows the surface valley low. ApRES repeat surveys are from 7 December 2019 to 22 December 2020. Negative melt denotes accretion.

#### 4.2. Bridging

Ice bridging is indicated in Figure 5c, as the basal shape is not mirrored directly at the surface. Surface changes shown in Figure 5d suggest that melt induced changes to the basal shape are also not mirrored directly at the surface, indicating bridging. The rigidity of ice distributes bridging stresses, whereby the weight of ice is partially supported laterally by the surrounding ice and ground. This smooths the surface response to basal changes at a length scale which masks small features. This is shown in Figure 7, where in places the surface is above flotation on the channel and close to or below flotation to either side of the channel. Over larger regions ( $\approx 1 \times 1$  km) the ice is adjusting to hydrostatic equilibrium, while over smaller length scales ( $\approx 100 \times 100$  m) the ice is not at flotation. This is well supported by ice dynamics theory, which predicts that the length scale of surface expressions of the basal channel will be no smaller than ice thickness (Figure S4 in Supporting Information S1,  $\approx 700$  m at the field site) (e.g., Gudmundsson & Raymond, 2008). Significant bridging has been noted around other ice shelf channels, and used to explain discrepancies between basal and surface topography (e.g., Chartrand & Howat, 2020; Dutrieux et al., 2013; Vaughan et al., 2012). These explanations are supported by ice dynamics modeling by Drews (2015), who found that narrow channels show significant bridging, even at equilibrium.

While further stress modeling would be required to understand in more detail where bridging stresses affect the surface expressions of the basal channel, our observations begin to explain how surface lowering is influenced by bridging. One conclusion is that more basal melt has occurred than that which is manifest in surface lowering. In our study area, ice is furthest from hydrostatic equilibrium at the inception of the channel (Figure 7), which is upstream from the surface valley (Figure 5c). We expect basal melt to occur at the start of a positive basal gradient of ice, as theoretical models of sub-ice-shelf plumes assume these plumes are generated by buoyancy (Jenkins, 1991). These models predict that positive slopes at the ice base, like that at the head of the channel, will generate melting. However, the region of surface lowering does not overlap the inception of the channel but starts 300 m downstream from the initial channel ramp (Figure 6). We attribute this discrepancy to ice bridging and suggest that melt is occurring at the inception of the basal channel but is not expressed at the surface. Significant bridging is expected at the inception as it is just 200 m wide (shown in Figure 5, similar to the channel modeled by Drews (2015) and Wearing et al. (2021)). As the channel inception grows wider over time, as it has downstream, basal melt will likely be more directly manifest as surface lowering. The approximately 2 km wide region of surface lowering (Figure 5d) is much wider than the 200–400 m wide basal channel below, reflecting the fact that sharp changes to the base will be smoothed at the surface due to bridging stresses which provide lateral support. While the area of the surface lowering may be larger than the area of basal melt, the volume of ice lowered on the surface is expected to be smaller than the basal volume melted due to lateral support in the ice. The surface change will also lag behind the basal melt in time. ApRES surveying shows basal accretion at the edge of the large area of surface lowering (Figures 3, 5, and 9). This likely shows that while basal melting and accretion are occurring within close proximity, the melt signal is overwhelmingly larger, and so is smoothed by bridging and masks the accretion signal at the surface.

### 4.3. Quantifying Basal Melt

Despite the distorted representation of basal changes on the surface topography, we know that basal topography will be underrepresented at the surface but not over represented. It follows that we can estimate a minimum melt rate from REMA differences (Section 3.2.1). REMA and ICESAT-2 elevation differences show surface downwasting of up to  $-1.8 \pm 0.4$  and  $-1.25 \pm 0.02$  m/a respectively. In the same location Kim et al. (2016) used Landsat imagery to calculate  $-1.2$  m/a of surface lowering. Integrating over the circular area of surface lowering shown in red in Figure 5c, the ice volume lost is found to be 3,000,000 m<sup>3</sup>/a. Calculating the submarine volume lost (assuming the lowering is from hydrostatic adjustment to equilibrium) and restricting the melted volume to the area of the intersection of the circle of surface lowering (Figure 5c) and the basal channel, basal melt rates are estimated as  $\approx 35$  m/a. In comparison, Marsh et al. (2016) and Stanton et al. (2013) used ApRES to measure melt rates of  $22.2 \pm 0.2$  and  $14.2$ – $24.5$  m/a in channels on the ice shelves of the Whillans Ice Stream and Pine Island Glacier respectively. Figure 7 shows the region of surface lowering (delineated in Figure 6b) is not at hydrostatic equilibrium but is likely close to it, shown by the fact that ice <1 km downstream, on either side of the channel (at  $-380$  km,  $-726$  km) is floating. The along-flow strain rate in the area is  $< 2 \times 10^{-6}$  m/a (Alley et al., 2018), which is too small to produce such large surface changes.

Our estimate likely underestimates melt. First, our estimate neglects surface mass balance which is likely positive in the surface valley, due to the fact hollows tend to be filled in by wind driven snow (e.g., Gow & Rowland, 1965). Second, due to bridging stresses, the basal melt is likely under-represented at the surface (Drews, 2015). Third, in calculating a 1D melt rate from a melt volume we assume melt spans the channel area. However, melt is likely restricted to a smaller area due to the Coriolis force which will cause the melt plume to trend to the true left wall (more detail in Section 4.4.3). A smaller melt area would correspond to a higher 1D melt rate for the same melt volume. Lastly, if the channel was filled with rock or till, similar to the channel surveyed by Drews et al. (2017), the assumption that the channel roof was supported by bridging or floating may be wrong, and melt rate could be overestimated. While sediment may play some role in the evolution of the channel, (as in Drews et al. (2017)), due to the location of the channel in a drainage outlet, the large magnitude of surface lowering, and the fact that the region of lowering ice is close to flotation (Figure 7), it is most likely that the channel is water filled.

The vertical accuracy of the 2012 and 2016 REMA strips is stated to be 4 and 3.5 m respectively (Howat et al., 2019; Noh & Howat, 2015). While 4 m is large relative to the  $\approx 5$  m range we observe to calculate the rate of surface lowering, it is unlikely we have overstated surface lowering considering our debiasing using contemporaneous CryoSat2 swath data. The REMA differencing is supported by ICESat-2, which has a mean accuracy

of 1.12 cm and shows a near identical region of lowering, with a similar magnitude (Figure S10 in Supporting Information S1). While the lowering shown in ICESat-2 spans a different time period, its similarities suggest that the process observed is ongoing. Over the more stable portion of the REMA strips the mean difference is  $-0.3 \pm 0.4$  m/a. In the region of lowering the mean surface change is  $-0.9 \pm 0.4$  m/a. The REMA differencing does exhibit banded artifacts but these are different in orientation to the observed lowering (Figure S12 in Supporting Information S1).

#### 4.4. Mechanisms

##### 4.4.1. Stepped Grounding Line Retreat

With ice velocity less than 5 m/a at the channel head (Rignot et al., 2017), there is no clear mechanism to explain why the basal channel is a long feature ( $>10$  km). We suggest that the melt plume has migrated upstream, leading to the present linear channel shape. In Section 4.3 we estimated modern melt rates to be over 35 m/a. At this rate, the basal channel would take approximately 10 years to melt vertically through 350 m of ice to its current height. The fact that melt is ongoing suggests that the channel exhibits large changes in melt rates, and/or the channel melt migrates over time. Landsat imagery shows the surface valley migrates upstream (Figure 4), and REMA differences reveal modern melt is likely at the head of the channel (Figure 5d). Since 1985, the surface valley has grown upstream by 1.5 km toward the location of modern surface lowering (Figure 4, 2020). Similarly, Chartrand and Howat (2020) observed a sub-ice-shelf basal channel migrating upstream toward a grounding line at  $\approx 1$  km/a. Surface elevation shows three distinct basins in the surface valley (B1, B2, B3, Figure 6). These basins are clear in the oldest satellite imagery of the valley (Figure 4, 1985). We interpret the surface basins to be historic plume locations and suggest that the modern grounding line and meltwater plume location is situated just upstream of the surface lowering shown in Figure 5d.

We suggest that the basin features are formed by varying melt from either or a combination of the two processes proposed by Horgan et al. (2017) to describe disjointed channel features in the area. Either melt rates vary in time or the region's grounding line has undergone stepwise retreat. Large changes in melt rates could result from changes in flux in the subglacially sourced meltwater plume. Changes in plume flux could be caused by episodic subglacial drainage events upstream, originating from the flooding of upstream active subglacial lakes as described by Kim et al. (2016), or in changes in flux caused by the rapid rerouting of the subglacial network as described by Carter and Fricker (2012). Maximums in subglacial outflow would create a stronger plume, melting the channel higher into the ice. In quiescent phases, melt would be focused lower in the water column on the channel walls, creating the wider parts of the channel associated with the surface basins we describe. While changes in ocean conditions could similarly cause fluctuations in melt rates due to the dependence of melt on the amount of heat and salt entrained from the ocean (Jenkins, 1991), conditions in the ice shelf cavity interior are expected to be stable (Stevens et al., 2020). Alternatively, the region's grounding line could be retreating episodically. At each step, the steep plume would melt a hollow, manifest in a basin shape on the ice surface. Stepwise retreat can occur when the grounding line jumps between stable positions usually determined by local bed topography (Haseloff & Sergienko, 2018), and is commonly observed (e.g., Jakobsson et al., 2012), although embayments as narrow as the one we observe here are seldom reported.

The channel bends and corresponding changes in channel width could be interpreted as channel meandering, similar to that of a supraglacial river (e.g., Ferguson, 1973). At these wider parts of the channel, the ice shelf has less buoyancy and so locally sinks, manifesting as the basins at the surface seen in Figure 5. We do not however think meandering is a robust explanation for the channel shape, as it is unlikely the plume melts down the length of the channel in a manner similar to a supraglacial river. First, the channel walls widen both left and right at bends rather than just on the outside of a bend like a supraglacial river (Ferguson, 1973). Second, plume theory predicts that downstream from the initial positive gradient of the channel, the plume will not melt basal ice. Past this point, the plume will either cause accretion, as observed in ApRES observations (Figure 9), or detach from the ice. It is possible that downstream from the positive gradient in ice basal slope at the head of the channel, subsequent plumes are generated from ice slopes on the walls or from downstream positive gradients in the channel depicted in Figure 6. The moniliform shape of the surface valley is similar to the shape of a feature observed by Berger et al. (2017) (Figure 7) at the Roi Baudouin ice shelf, Antarctica. Radar imagery shows this is the surface expression of englacial lakes found 30 m below the surface. While the basins we see are not formed by



englacial lakes, it is interesting to note that this shape of connected basins in ice shelf topography appears to be stable.

Horgan et al. (2017) propose that the grounding line retreated to its current location after the stagnation of the Kamb Ice Stream. Due to its location in a hydropotential low (Le Brocq et al., 2009), the basal channel likely existed under grounded ice before Kamb Ice Stream's stagnation. Once the grounding line retreated to its current location, an increase in melt and low rates of creep closure in the ice likely allowed the channel to grow to its current size. Melt likely increased due to the proximity to the ocean, and increase in supply of salty bottom water. Feedbacks between plume development, channel formation and ocean entrainment (as described by Sergienko (2013)) would have drawn more salt water to the ice base, increasing melt rates. Once ice advection stopped, even if melt rates were low, the plume would be concentrated in one location allowing it to incise a deep channel. It is most likely that the channel then migrated upstream. With no upstream migration of the channel, the observed 10 km long surveyed section of the basal channel would take approximately 2000 years to form through advection with present ice velocity ( $\approx 5$  m/a), which does not align with the time scale of the change in grounding line position ( $<150$  years).

It is possible that a strengthening of the meltwater plume is related to a proposed reorganization of the subglacial drainage system (e.g., Anandakrishnan & Alley, 1997), which may be associated with the ice stream shut down around 150 years ago. For example, if the subglacial hydrology of the Kamb ice stream became more channelized as proposed by Lelandais et al. (2018), subglacial water flux at this location would increase. More buoyant subglacial water would be discharged at the grounding line, likely strengthening the sub-ice-shelf plume.

#### 4.4.2. Steep Initial Channel Slope

The initial gradient of the ice base at the inception of the channel in the downstream direction is constrained between  $45^\circ$  and  $90^\circ$  by radar echo sounding observations (Figure 6). This implies that the plume was flowing upwards at a steep or vertical angle when it incised the head of the channel. We suggest that the channel grows through a positive feedback between basal steepness and melt as described by Sergienko (2013) and Gladish et al. (2012). Through this feedback, steep basal slopes cause the plume flow to accelerate, which causes more melt, making preexisting slopes even steeper. In other observed ice shelf channels (e.g., Drews et al., 2017; Jeofry et al., 2018), the height of incision is moderated by ice advection which restricts the amount of time any region on the ice shelf base experiences melt. In our study location, ice velocity is less than 5 m/a (Rignot et al., 2017). Any notch melted into the ice shelf is not advected downstream but grows deeper over time, resulting in a steep gradient at the channel inception. Unless the plume changes, the feedback between slope and melting can continue until the channel is vertical at its inception (Gladish et al., 2012; Sergienko, 2013). The roof of the basal channel follows roughly the same elevation of  $\approx -380$  m (Figure 6). This may represent a natural limit to which the freshwater plume will rise given the ocean density structure. A natural bound on the roof of the channel should correspond to the height at which the plume reaches the density of the surrounding sea. Here, melt-water plumes are expected to stop rising and detach from the ice, flowing horizontally into the sea (Hewitt, 2020; Jenkins, 2011). Direct access oceanographic investigations of the channel, completed in the 2021–2022 field season will provide further insight to plume flow.

#### 4.4.3. Lateral Channel Migration

Both REMA (Figure 5d) and ICESat-2 data (Figures 8g–8l), shows less negative surface lowering (relative raising) just to the true right of the surface expression apex, and more negative surface lowering (relative lowering) on the true left of the surface apex. The relative rising surface is likely related to the accretion shown at the base of the channel by our ApRES observations (Figure 9), which indicate more accretion is occurring on the true right of the channel. This is coincident with a ledge (L2, Figures S8 in Supporting Information S1) described in Section 3.1.2. The Coriolis force likely causes the melt plume to follow the true left wall. This may be accompanied by accretion on the true right side, resulting in the leftward migration of the channel. While it is not commonly observed that channels migrate to the left, Gourmelen et al. (2017) and Alley et al. (2016) found steeper walls on the true left of channel profiles and attributed the asymmetry to enhanced melt due to the Coriolis force. Similarly, Chartrand and Howat (2020) observed the leftward migration of a channel at  $\approx 80$  m/a. Our basal channel profiles show asymmetry in that the channel has large ledges on the right hand side for roughly half of the distance down the channel (Figures S8 and S9 in Supporting Information S1). Ledges (terraces) were also

found on an ice shelf channel by Dutrieux et al. (2014), who attributed the ledges to channel melt. It is likely that the ledges we observe have previously formed through melt. As the channel migrated upstream and shifted the meltwater plume further from the location of the ledges, the ledges may have shifted from a melt regime to one of accretion, or accumulation of frazil. Drews et al. (2020) also observed a pattern of surface lowering and raising across an ice shelf channel, and interpreted this pattern to be caused by wind eroding snow from windward slopes and depositing it on the leeward side of slopes.

Relative to the ApRES data, REMA and ICESat-2 observations of a rising surface span a different time period and location respectively. However, both REMA and ICESat-2 show a consistent trend of a rising surface on the channel right (Figures 5d and 8g–8i). In REMA difference data, this observed raising is the same sign as a portion of the REMA strip (Figures S11 and S12 in Supporting Information S1), increasing the likelihood that the observations are artifacts. However, the close coincidence of similar raising in the more accurate ICESat-2 data supports the observation. ApRES accretion and the surface raising shown in REMA and ICESat-2 occur downstream from the region of surface lowering we attribute to melt (Figure 5d). This agrees with plume theory, which predicts that as a plume loses energy it causes accretion downstream from where melt is occurring Jenkins (1991). Estimating the location of accretion with the 1D model of Jenkins (2011) is not done here as the oceanographic variables (e.g. ambient stratification in the ocean cavity) are unknown to us, and result in large changes in the length scale over which accretion occurs.

## 5. Conclusion

We have presented a series of observations describing a sub-ice-shelf channel at the grounding line of Kamb Ice Stream, combining remote sensing and field-based geophysical surveying. We used these observations to constrain theories of ice and ocean interaction in the channel, and processes which have formed the channel. Observations reveal that the channel is actively melting at its upstream inception point and has been growing upstream past the grounding line since at least 1985. The inferred melt is likely driven by a buoyant plume, initiated by freshwater from Kamb Ice Stream's largest subglacial drainage outlet. The channel is asymmetric and tortuous. While most sub-ice-shelf channels are formed as downstream streak lines in advecting ice, the channel we present is situated in stagnant ice, and appears to have developed its elongated shape due to a shift in the melt location. Oversnow radar surveying shows that the channel widens 50%–100% at each bend. The bends correspond to a series of basins on the surface which we relate to past periods of continuous melt. We interpret the bends and basins as evidence that the upstream migration of the melt location at the head of the channel is irregular, stepping upstream over time. This irregularity likely stems from episodic subglacial drainage and/or instabilities in grounding line locations associated with bed topography. Radar surveying reveals that the channel inception extends 300 m upstream from its surface expression. The upstream 300 m of the channel is narrow (250 m wide) and is not floating but is supported by bridging to the flanks of the channel. Satellite products reveal basal melt manifest as surface lowering. By quantifying this surface lowering, we estimate melt to be at least 35 m/a. In agreement with channel theory, melt occurs near the upstream inception of the channel, and ice is accreted onto the channel roof downstream. This accretion is verified with ApRES observations and appears to be contributing to the growth of a ledge in the channel. The differences between the surface expression and basal features of this channel are noteworthy for studies of sub-ice-shelf channels using surface observations alone. To predict the stability of ice shelves, it may be important to model sub-ice-shelf channels. Our observations can be used as a case study to further constrain theories of channel formation and growth. As the channel shape is not distorted by advection, it serves as a natural experiment for understanding plume driven melt. The results presented show that melt can form an ice shelf channel in the absence of advection through the inland migration of a focused melt source. Migration has continued upstream from the local grounding line, with melt driven by the upstream transport of salt water through circulation likely similar to an estuarine river mouth. The focused melt source appears to continue to deepen and steepen the channel at its inception. Future research on this channel could build on the work of this paper by better constraining melt rates and ocean plume properties, which in turn could be used to better understand both the impact of channels and ice shelves, and subglacial discharge. This was the objective of a direct access drilling campaign carried out in the austral summer of 2021/2022.

## Data Availability Statement

Low frequency and ApRES radar data and ice thickness product are available at Zenodo via (<https://doi.org/10.5281/zenodo.5574647>). Accompanying code and notebooks are available at GitHub via ([https://github.com/arran/PhD\\_data\\_chapter](https://github.com/arran/PhD_data_chapter)).

## Acknowledgments

This research was funded by the Aotearoa New Zealand Antarctic Science Platform (ANTA1801) Antarctic Ice Dynamics Project (ASP02101), and the NZARI Ross Ice Shelf Project. HH and AW were supported by a Royal Society of New Zealand Rutherford Discovery Fellowship (Contract: RDF-VUW1602). The equipment used to collect the low-frequency radar data was lent by Ginny Catania (Jackson School of Geosciences, University of Texas in Austin). Greg Leonard and Kelly Gragg (School of Surveying, University of Otago) assisted with the radar set-up. Our thanks to Antarctica New Zealand for the field support which was critical to the success of this research. Open access publishing facilitated by Victoria University of Wellington, as part of the Wiley - Victoria University of Wellington agreement via the Council of Australian University Librarians.

## References

- Alley, K. E., Scambos, T. A., Alley, R. B., & Holschuh, N. (2019). Troughs developed in ice-stream shear margins precondition ice shelves for ocean-driven breakup. *Science Advances*, 5(10), eaax2215. <https://doi.org/10.1126/sciadv.aax2215>
- Alley, K. E., Scambos, T. A., Anderson, R. S., Rajaram, H., Pope, A., & Haran, T. M. (2018). Continent-wide estimates of Antarctic strain rates from Landsat 8-derived velocity grids. *Journal of Glaciology*, 64(244), 321–332. <https://doi.org/10.1017/jog.2018.23>
- Alley, K. E., Scambos, T. A., Siegfried, M. R., & Fricker, H. A. (2016). Impacts of warm water on Antarctic ice shelf stability through basal channel formation. *Nature Geoscience*, 9(4), 290–293. <https://doi.org/10.1038/ngeo2675>
- Anandakrishnan, S., & Alley, R. B. (1997). Stagnation of ice stream C, West Antarctica by water piracy. *Geophysical Research Letters*, 24(3), 265–268. <https://doi.org/10.1029/96GL04016>
- Arnold, E., Leuschen, C., Rodriguez-Morales, F., Li, J., Paden, J., Hale, R., & Keshmiri, S. (2020). CREIS airborne radars and platforms for ice and snow sounding. *Annals of Glaciology*, 61(81), 58–67. <https://doi.org/10.1017/aog.2019.37>
- Berger, S., Drews, R., Helm, V., Sun, S., & Pattyn, F. (2017). Detecting high spatial variability of ice shelf basal mass balance, Roi Baudouin Ice Shelf, Antarctica. *The Cryosphere*, 11(6), 2675–2690. <https://doi.org/10.5194/tc-2017-41>
- Berthier, E., Scambos, T. A., & Shuman, C. A. (2012). Mass loss of Larsen B tributary glaciers (Antarctic Peninsula) unabated since 2002. *Geophysical Research Letters*, 39(13). <https://doi.org/10.1029/2012gl0151755>
- Brennan, P. V., Lok, L. B., Nicholls, K., & Corr, H. (2014). Phase-sensitive FMCW radar system for high-precision Antarctic ice shelf profile monitoring. *IET Radar, Sonar & Navigation*, 8(7), 776–786. <https://doi.org/10.1049/iet-rsn.2013.0053>
- Carter, S., & Fricker, H. (2012). The supply of subglacial meltwater to the grounding line of the Siple Coast, West Antarctica. *Annals of Glaciology*, 53(60), 267–280. <https://doi.org/10.3189/2012aog60a119>
- Chartrand, A., & Howat, I. (2020). Basal Channel evolution on the Getz Ice Shelf, West Antarctica. *Journal of Geophysical Research: Earth Surface*, 125(9), e2019JF005293. <https://doi.org/10.1029/2019jef005293>
- Christianon, K., Jacobel, R. W., Horgan, H. J., Alley, R. B., Anandakrishnan, S., Holland, D. M., & DallaSanta, K. J. (2016). Basal conditions at the grounding zone of Whillans Ice Stream, West Antarctica, from ice-penetrating radar. *Journal of Geophysical Research: Earth Surface*, 121(11), 1954–1983. <https://doi.org/10.1002/2015jef003806>
- Corr, H. F., Jenkins, A., Nicholls, K. W., & Doake, C. (2002). Precise measurement of changes in ice-shelf thickness by phase-sensitive radar to determine basal melt rates. *Geophysical Research Letters*, 29(8), 73–81. <https://doi.org/10.1029/2001gl014618>
- Cramer, F. (2018). Scientific colour maps. *Zenodo*. <https://doi.org/10.5281/zenodo.1243862>
- Depoorter, M. A., Bamber, J. L., Griggs, J. A., Lenaerts, J. T., Ligtenberg, S. R., van den Broeke, M. R., & Moholdt, G. (2013). Calving fluxes and basal melt rates of Antarctic ice shelves. *Nature*, 502(7469), 89–92. <https://doi.org/10.1038/nature12567>
- Dowdeswell, J. A., & Evans, S. (2004). Investigations of the form and flow of ice sheets and glaciers using radio-echo sounding. *Reports on Progress in Physics*, 67(10), 1821–1861. <https://doi.org/10.1088/0034-4885/67/10/r03>
- Drews, R. (2015). Evolution of ice-shelf channels in Antarctic ice shelves. *The Cryosphere*, 9(3), 1169–1181. <https://doi.org/10.5194/tc-9-1169-2015>
- Drews, R., Pattyn, F., Hewitt, I., Ng, F., Berger, S., Matsuoka, K., et al. (2017). Actively evolving subglacial conduits and eskers initiate ice shelf channels at an Antarctic grounding line. *Nature Communications*, 8(1), 15228. <https://doi.org/10.1038/ncomms15228>
- Drews, R., Schannwell, C., Ehlers, T., Gladstone, R., Pattyn, F., & Matsuoka, K. (2020). Atmospheric and oceanographic signatures in the Ice-Shelf Channel Morphology of Roi Baudouin Ice Shelf, East Antarctica, inferred from radar data. *Journal of Geophysical Research: Earth Surface*, 125(7), e2020JF005587. <https://doi.org/10.1029/2020jef005587>
- Dupont, T., & Alley, R. (2005). Assessment of the importance of ice-shelf buttressing to ice-sheet flow. *Geophysical Research Letters*, 32(4). <https://doi.org/10.1029/2004gl020224>
- Dutrieux, P., Stewart, C. L., Jenkins, A., Nicholls, K. W., Corr, H. F., Rignot, E., & Steffen, K. (2014). Basal terraces on melting ice shelves. *Geophysical Research Letters*, 41(15), 5506–5513. <https://doi.org/10.1002/2014gl060618>
- Dutrieux, P., Vaughan, D. G., Corr, H. F., Jenkins, A., Holland, P. R., Joughin, I., & Fleming, A. (2013). Pine Island glacier ice shelf melt distributed at kilometre scales. *The Cryosphere*, 7(5), 1543–1555. <https://doi.org/10.5194/tc-7-1543-2013>
- Edwards, T. L., Nowicki, S., Marzeion, B., Hock, R., Goelzer, H., Seroussi, H., et al. (2021). Projected land ice contributions to twenty-first-century sea level rise. *Nature*, 593(7857), 74–82.
- Engelhardt, H., & Kamb, B. (1997). Basal hydraulic system of a West Antarctic ice stream: Constraints from borehole observations. *Journal of Glaciology*, 43(144), 207–230. <https://doi.org/10.1017/s0022143000003166>
- Ferguson, R. (1973). Sinuosity of supraglacial streams. *The Geological Society of America Bulletin*, 84(1), 251–256. [https://doi.org/10.1130/0016-7606\(1973\)84<251:soas>2.0.co;2](https://doi.org/10.1130/0016-7606(1973)84<251:soas>2.0.co;2)
- Fried, M., Hulbe, C., & Fahnestock, M. (2014). Grounding-line dynamics and margin lakes. *Annals of Glaciology*, 55(66), 87–96. <https://doi.org/10.3189/2014aog66a216>
- Fürst, J. J., Durand, G., Gillet-Chaulet, F., Tavaré, L., Rankl, M., Braun, M., & Gagliardini, O. (2016). The safety band of Antarctic ice shelves. *Nature Climate Change*, 6(5), 479–482. <https://doi.org/10.1038/nclimate2912>
- Gladish, C. V., Holland, D. M., Holland, P. R., & Price, S. F. (2012). Ice-shelf basal channels in a coupled ice/ocean model. *Journal of Glaciology*, 58(212), 1227–1244. <https://doi.org/10.3189/2012jog12j003>
- Goeller, S., Helm, V., Thoma, M., & Grosfeld, K. (2015). Subglacial hydrology indicates a major shift in dynamics of the West Antarctic Ross Ice Streams within the next two centuries. *The Cryosphere Discussions*, 9(4), 3995–4018.
- Goldberg, D., Gourmelen, N., Kimura, S., Millan, R., & Snow, K. (2019). How accurately should we model ice shelf melt rates? *Geophysical Research Letters*, 46(1), 189–199. <https://doi.org/10.1029/2018gl080383>
- Gourmelen, N., Escorihuela, M., Shepherd, A., Foresta, L., Muir, A., Garcia-Mondéjar, A., et al. (2018). CryoSat-2 swath interferometric altimetry for mapping ice elevation and elevation change. *Advances in Space Research*, 62(6), 1226–1242. <https://doi.org/10.1016/j.asr.2017.11.014>

- Gourmelen, N., Goldberg, D. N., Snow, K., Henley, S. F., Bingham, R. G., Kimura, S., et al. (2017). Channelized melting drives thinning under a rapidly melting Antarctic ice shelf. *Geophysical Research Letters*, 44(19), 9796–9804. <https://doi.org/10.1002/2017gl074929>
- Gow, A. J., & Rowland, R. (1965). On the relationship of snow accumulation to surface topography at “Byrd Station” Antarctica. *Journal of Glaciology*, 5(42), 843–847. <https://doi.org/10.3189/s0022143000018906>
- Gudmundsson, G. H., & Raymond, M. (2008). On the limit to resolution and information on basal properties obtainable from surface data on ice streams. *The Cryosphere*, 2(2), 167–178. <https://doi.org/10.5194/tc-2-167-2008>
- Haran, T., Bohlander, J., Scambos, T., Painter, T., & Fahnestock, M. (2014). *MODIS Mosaic of Antarctica 2008–2009 (MOA2009) image map* (Vol. 10, p. N5KP8037). National Snow and Ice Data Center.
- Haseloff, M., & Sergienko, O. V. (2018). The effect of buttressing on grounding line dynamics. *Journal of Glaciology*, 64(245), 417–431. <https://doi.org/10.1017/jog.2018.30>
- Herron, M. M., & Langway, C. C. (1980). Firn densification: An empirical model. *Journal of Glaciology*, 25(93), 373–385. <https://doi.org/10.1017/s0022143000015239>
- Hewitt, I. J. (2020). Subglacial plumes. *Annual Review of Fluid Mechanics*, 52(1), 145–169. <https://doi.org/10.1146/annurev-fluid-010719-060252>
- Horgan, H., Hulbe, C., Alley, R., Anandakrishnan, S., Goodsell, B., Taylor-Offord, S., & Vaughan, M. (2017). Poststagnation retreat of Kamb Ice Stream’s grounding zone. *Geophysical Research Letters*, 44(19), 9815–9822. <https://doi.org/10.1002/2017gl074986>
- Howat, I. M., Porter, C., Smith, B. E., Noh, M.-J., & Morin, P. (2019). The reference elevation model of Antarctica. *The Cryosphere*, 13(2), 665–674. <https://doi.org/10.5194/tc-13-665-2019>
- Hulbe, C. L., & Fahnestock, M. A. (2004). West Antarctic ice-stream discharge variability: Mechanism, controls and pattern of grounding-line retreat. *Journal of Glaciology*, 50(171), 471–484. <https://doi.org/10.3189/172756504781829738>
- Jacobel, R. W., Welch, B. C., Osterhouse, D., Pettersson, R., & MacGregor, J. A. (2009). Spatial variation of radar-derived basal conditions on Kamb Ice Stream, West Antarctica. *Annals of Glaciology*, 50(51), 10–16. <https://doi.org/10.3189/172756409789097504>
- Jacobs, S., Helmer, H., Doake, C., Jenkins, A., & Frolich, R. (1992). Melting of ice shelves and the mass balance of Antarctica. *Journal of Glaciology*, 38(130), 375–387. <https://doi.org/10.1017/s0022143000002252>
- Jacobs, S. S., Gordon, A. L., & Ardai, J. (1979). Circulation and melting beneath the Ross Ice Shelf. *Science*, 203(4379), 439–443. <https://doi.org/10.1126/science.203.4379.439>
- Jakobsson, M., Anderson, J. B., Nitsche, F. O., Gyllencreutz, R., Kirshner, A. E., Kirchner, N., et al. (2012). Ice sheet retreat dynamics inferred from glacial morphology of the central Pine Island Bay Trough, West Antarctica. *Quaternary Science Reviews*, 38, 1–10. <https://doi.org/10.1016/j.quascirev.2011.12.017>
- Jenkins, A. (1991). A one-dimensional model of ice shelf-ocean interaction. *Journal of Geophysical Research*, 96(C11), 20671–20677. <https://doi.org/10.1029/91jc01842>
- Jenkins, A. (2011). Convection-driven melting near the grounding lines of ice shelves and tidewater glaciers. *Journal of Physical Oceanography*, 41(12), 2279–2294. <https://doi.org/10.1175/jpo-d-11-03.1>
- Jeofry, H., Ross, N., Le Brocq, A., Graham, A. G., Li, J., Gogineni, P., et al. (2018). Hard rock landforms generate 130 km ice shelf channels through water focusing in basal corrugations. *Nature Communications*, 9(1), 1–9. <https://doi.org/10.1038/s41467-018-06679-z>
- Kim, B.-H., Lee, C.-K., Seo, K.-W., Lee, W. S., & Scambos, T. (2016). Active subglacial lakes and channelized water flow beneath the Kamb Ice Stream. *The Cryosphere*, 10(6), 2971–2980. <https://doi.org/10.5194/tc-10-2971-2016>
- Le Brocq, A. M., Payne, A., Siegert, M., & Alley, R. B. (2009). A subglacial water-flow model for West Antarctica. *Journal of Glaciology*, 55(193), 879–888. <https://doi.org/10.3189/002214309790152564>
- Le Brocq, A. M., Ross, N., Griggs, J. A., Bingham, R. G., Corr, H. F., Ferraccioli, F., et al. (2013). Evidence from ice shelves for channelized meltwater flow beneath the Antarctic Ice Sheet. *Nature Geoscience*, 6(11), 945–948. <https://doi.org/10.1038/ngeo1977>
- Lelandais, T., Ravier, É., Pochat, S., Bourgeois, O., Clark, C., Mourgues, R., & Strzeczynski, P. (2018). Modelled subglacial floods and tunnel valleys control the life cycle of transitory ice streams. *The Cryosphere*, 12(8), 2759–2772. <https://doi.org/10.5194/tc-12-2759-2018>
- Lenaerts, J. T., Van den Broeke, M., Van de Berg, W., Van Meijgaard, E., & Kuipers Munneke, P. (2012). A new, high-resolution surface mass balance map of Antarctica (1979–2010) based on regional atmospheric climate modelling. *Geophysical Research Letters*, 39(4). <https://doi.org/10.1029/2011gl050713>
- Lewis, E., & Perkin, R. (1986). Ice pumps and their rates. *Journal of Geophysical Research*, 91(C10), 11756–11762. <https://doi.org/10.1029/jc091ic10p11756>
- Liu, Y., Moore, J. C., Cheng, X., Gladstone, R. M., Bassis, J. N., Liu, H., et al. (2015). Ocean-driven thinning enhances iceberg calving and retreat of Antarctic ice shelves. *Proceedings of the National Academy of Sciences*, 112(11), 3263–3268. <https://doi.org/10.1073/pnas.1415137112>
- MacAyeal, D. R. (1984). Thermohaline circulation below the Ross Ice Shelf: A consequence of tidally induced vertical mixing and basal melting. *Journal of Geophysical Research*, 89(C1), 597–606. <https://doi.org/10.1029/jc089ic01p00597>
- MacAyeal, D. R. (1985). Evolution of tidally triggered meltwater plumes below ice shelves. *Oceanology of the Antarctic Continental Shelf*, 43, 133–143. <https://doi.org/10.1029/ar043p0133>
- Mankoff, K. D., Jacobs, S. S., Tulaczyk, S. M., & Stammerjohn, S. E. (2012). The role of Pine Island Glacier ice shelf basal channels in deep-water upwelling, polynyas and ocean circulation in Pine Island Bay, Antarctica. *Annals of Glaciology*, 53(60), 123–128. <https://doi.org/10.3189/2012aog60a062>
- Marsh, O. J., Fricker, H. A., Siegfried, M. R., Christianson, K., Nicholls, K. W., Corr, H. F., & Catania, G. (2016). High basal melting forming a channel at the grounding line of Ross Ice Shelf, Antarctica. *Geophysical Research Letters*, 43(1), 250–255. <https://doi.org/10.1002/2015gl066612>
- Millgate, T., Holland, P. R., Jenkins, A., & Johnson, H. L. (2013). The effect of basal channels on oceanic ice-shelf melting. *Journal of Geophysical Research: Oceans*, 118(12), 6951–6964. <https://doi.org/10.1002/2013jc009402>
- Mouginot, J., Rignot, E., & Scheuchl, B. (2019). Continent-wide, interferometric SAR phase, mapping of Antarctic ice velocity. *Geophysical Research Letters*, 46(16), 9710–9718. <https://doi.org/10.1029/2019gl083826>
- Natural Resources Canada. (2016). Natural Resources Canada’s online tool Canadian Spatial Reference System-precise point positioning (PPP) [Computer software manual].
- Ng, F., & Conway, H. (2004). Fast-flow signature in the stagnated Kamb Ice Stream, West Antarctica. *Geology*, 32(6), 481–484. <https://doi.org/10.1130/g20317.1>
- Nicholls, K. W., Corr, H. F., Stewart, C. L., Lok, L. B., Brennan, P. V., & Vaughan, D. G. (2015). A ground-based radar for measuring vertical strain rates and time-varying basal melt rates in ice sheets and shelves. *Journal of Glaciology*, 61(230), 1079–1087. <https://doi.org/10.3189/2015jog15j073>
- Noh, M.-J., & Howat, I. M. (2015). Automated stereo-photogrammetric DEM generation at high latitudes: Surface Extraction with TIN-based Search-space Minimization (SETSM) validation and demonstration over glaciated regions. *GIScience and Remote Sensing*, 52(2), 198–217. <https://doi.org/10.1080/15481603.2015.1008621>



- Retzlaff, R., & Bentley, C. R. (1993). Timing of stagnation of Ice Stream C, West Antarctica from short-pulse-radar studies of buried surface crevasses. *Journal of Glaciology*, 39(133), 553–561. <https://doi.org/10.1017/s0022143000016440>
- Rignot, E., Bamber, J. L., Van Den Broeke, M. R., Davis, C., Li, Y., Van De Berg, W. J., & Van Meijgaard, E. (2008). Recent Antarctic ice mass loss from radar interferometry and regional climate modelling. *Nature Geoscience*, 1(2), 106–110. <https://doi.org/10.1038/ngeo102>
- Rignot, E., Casassa, G., Gogineni, P., Krabill, W., Rivera, A., & Thomas, R. (2004). Accelerated ice discharge from the Antarctic Peninsula following the collapse of Larsen B ice shelf. *Geophysical Research Letters*, 31(18), L18401. <https://doi.org/10.1029/2004gl020697>
- Rignot, E., Jacobs, S., Mouginot, J., & Scheuchl, B. (2013). Ice-shelf melting around Antarctica. *Science*, 341(6143), 266–270. <https://doi.org/10.1126/science.1235798>
- Rignot, E., Mouginot, J., & Scheuchl, B. (2017). *MEaSUREs InSAR-based Antarctica ice velocity map, version 2*. NASA National Snow and Ice Data Center Distributed Active Archive Center. <https://doi.org/10.5067/D7GK8F5J8M8R>
- Rignot, E., & Steffen, K. (2008). Channelized bottom melting and stability of floating ice shelves. *Geophysical Research Letters*, 35(2), L02503. <https://doi.org/10.1029/2007gl031765>
- Roy, D., Wulder, M., Loveland, T., Woodcock, C. E., Allen, R., Anderson, M., et al. (2014). Landsat-8: Science and product vision for terrestrial global change research. *Remote Sensing of Environment*, 145, 154–172. <https://doi.org/10.1016/j.rse.2014.02.001>
- Scambos, T. A., Bohlander, J. A., Shuman, C. A., & Skvarca, P. (2004). Glacier acceleration and thinning after ice shelf collapse of the Larsen B embayment, Antarctica. *Geophysical Research Letters*, 31(18), L18402. <https://doi.org/10.1029/2004gl020670>
- Sergienko, O. (2013). Basal channels on ice shelves. *Journal of Geophysical Research: Earth Surface*, 118(3), 1342–1355. <https://doi.org/10.1002/jgrf.20105>
- Smith, B., Dickinson, S., Jelley, B., Neumann, T., Hancock, D., Lee, J., & Harbeck, K. (2021). ATLAS/ICESat-2 L3B annual land ice height, version 3 [Computer Software Manual].
- Stanton, T. P., Shaw, W., Truffer, M., Corr, H., Peters, L., Riverman, K., et al. (2013). Channelized ice melting in the ocean boundary layer beneath Pine Island Glacier, Antarctica. *Science*, 341(6151), 1236–1239. <https://doi.org/10.1126/science.1239373>
- Stevens, C., Hulbe, C., Brewer, M., Stewart, C., Robinson, N., Ohneiser, C., & Jendersie, S. (2020). Ocean mixing and heat transport processes observed under the Ross Ice Shelf control its basal melting. *Proceedings of the National Academy of Sciences*, 117(29), 16799–16804. <https://doi.org/10.1073/pnas.1910760117>
- Stewart, C. L., Christoffersen, P., Nicholls, K. W., Williams, M. J., & Dowdeswell, J. A. (2019). Basal melting of Ross Ice Shelf from solar heat absorption in an ice-front polynya. *Nature Geoscience*, 12(6), 435–440. <https://doi.org/10.1038/s41561-019-0356-0>
- Uieda, L., Tian, D., Leong, W., Toney, L., Schlitzer, W., Grund, M., et al. (2021). *PyGMT: A Python interface for the generic mapping tools*. Python.
- Vaňková, I., Nicholls, K. W., & Corr, H. F. (2021). The nature of ice intermittently accreted at the base of Ronne Ice Shelf, Antarctica, assessed using phase-sensitive radar. *Journal of Geophysical Research: Oceans*, 126(10), e2021JC017290. <https://doi.org/10.1029/2021jc017290>
- Vaňková, I., Nicholls, K. W., Corr, H. F., Makinson, K., & Brennan, P. V. (2020). Observations of tidal melt and vertical strain at the Filchner-Ronne Ice Shelf, Antarctica. *Journal of Geophysical Research: Earth Surface*, 125(1), e2019JF005280. <https://doi.org/10.1029/2019jf005280>
- Vaughan, D. G., Corr, H. F., Bindshadler, R. A., Dutrieux, P., Gudmundsson, G. H., Jenkins, A., et al. (2012). Subglacial melt channels and fracture in the floating part of Pine Island Glacier, Antarctica. *Journal of Geophysical Research*, 117(F3). <https://doi.org/10.1029/2012jf002360>
- Wearing, M., Stevens, L., Dutrieux, P., & Kingslake, J. (2021). Ice-shelf basal melt channels stabilized by secondary flow. *Geophysical Research Letters*, 48(21), e2021GL094872. <https://doi.org/10.1029/2021gl094872>
- Wessel, P., Luis, J., Uieda, L., Scharroo, R., Wobbe, F., Smith, W., & Tian, D. (2019). The generic mapping tools version 6. *Geochemistry, Geophysics, Geosystems*, 20(11), 5556–5564. <https://doi.org/10.1029/2019gc008515>
- Young, T. J., Schroeder, D. M., Christoffersen, P., Lok, L. B., Nicholls, K. W., Brennan, P. V., et al. (2018). Resolving the internal and basal geometry of ice masses using imaging phase-sensitive radar. *Journal of Glaciology*, 64(246), 649–660. <https://doi.org/10.1017/jog.2018.54>

## References From the Supporting Information

- Wessel, P., & Smith, W. H. (1998). New, improved version of Generic Mapping Tools released. *Eos, Transactions American Geophysical Union*, 79(47), 579.